

AD-A254 130



Defense Nuclear Agency
Alexandria, VA 22310-3398



DNA-TR-92-17

Turbulent Dusty Boundary Layer in an ANFO Surface-Burst Explosion

Logicon RDA
P.O. Box 92500
Los Angeles, CA 90009

Lawrence Livermore National Laboratory
5230 Pacific Concourse Drive, Suite 200
Los Angeles, CA 90045

August 1992

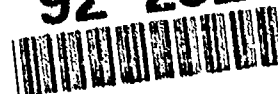
DTIC
ELECTE
AUG 21 1992
S A D

Technical Report

CONTRACT Nos. DNA-IACRO-91-853
DNA-MIPR-91-658
DNA 001-80-C-0046

Approved for public release;
distribution is unlimited.

92-23270



92 8 20 055

Destroy this report when it is no longer needed. Do not return to sender.

PLEASE NOTIFY THE DEFENSE NUCLEAR AGENCY,
ATTN: CSTI, 6801 TELEGRAPH ROAD, ALEXANDRIA, VA
22310-3398, IF YOUR ADDRESS IS INCORRECT, IF YOU
WISH IT DELETED FROM THE DISTRIBUTION LIST, OR
IF THE ADDRESSEE IS NO LONGER EMPLOYED BY YOUR
ORGANIZATION.



REPORT DOCUMENTATION PAGE

Form Approved
OMB No. 0704-0188

Public reporting burden for this collection of information is estimated to average 1 hour per response including the time for reviewing instructions, searching existing data sources, gathering and maintaining the data needed, and completing and reviewing the collection of information. Send comments regarding this burden estimate or any other aspect of this collection of information, including suggestions for reducing this burden, to Washington Headquarters Services, Directorate for Information Operations and Reports, 1215 Jefferson Davis Highway, Suite 1204, Arlington, VA 22202-4302, and to the Office of Management and Budget, Paperwork Reduction Project (0704-0188), Washington, DC 20503

1. AGENCY USE ONLY (Leave blank)		2. REPORT DATE 920801	3. REPORT TYPE AND DATES COVERED Technical 880101 - 891231	
4. TITLE AND SUBTITLE Turbulent Dusty Boundary Layer in an ANFO Surface-Burst Explosion			5. FUNDING NUMBERS C - DNA IACRO-91-853 DNA MIPR-91-658 DNA 001-88-C-0046 PE -62715H TR -RD TA - RC WU-DH999801	
6. AUTHOR(S) Allen L. Kuhl (Consultant, Logicon RDA), R. E. Ferguson, K. -Y. Chien, and J. P. Collins (NSWC)				
7. PERFORMING ORGANIZATION NAME(S) AND ADDRESS(ES) Logicon RDA Lawrence Livermore National Laboratory P.O. Box 92500 5230 Pacific Concourse Drive, Suite 200 Los Angeles, CA 90009 Los Angeles, CA 90045			8. PERFORMING ORGANIZATION REPORT NUMBER RDA-TR-0263229003-002	
9. SPONSORING/MONITORING AGENCY NAME(S) AND ADDRESS(ES) Defense Nuclear Agency 6801 Telegraph Road Alexandria, VA 22310-3398 SPWE/Peterson			10. SPONSORING/MONITORING AGENCY REPORT NUMBER DNA-TR-92-17	
11. SUPPLEMENTARY NOTES This work was sponsored by the Defense Nuclear Agency under RDT&E RMC Code B4662D RD RC 00016 DFPR 1910A 25904D.				
12a. DISTRIBUTION/AVAILABILITY STATEMENT Approved for public release; distribution is unlimited.			12b. DISTRIBUTION CODE	
13. ABSTRACT (Maximum 200 words) This paper describes the results of numerical simulations of the dusty, turbulent boundary layer created by a surface burst explosion. The blast wave was generated by the detonation of a 600-T hemisphere of ANFO, similar to those used in large-scale field tests. The surface was assumed to be ideally noncratering but contained an initial loose layer of dust. The dust-air mixture in this fluidized bed was modeled as a dense gas (i.e., an equilibrium model, valid for very-small-diameter dust particles). The evolution of the flow was calculated by a high-order Godunov code that solves the nonsteady conservation laws. Shock interactions with dense layer generated vorticity near the wall—similar to viscous, no-slip effects found in clean flows. The resulting wall shear layer was unstable, and rolled up into large-scale rotational structures. These structures entrained dense material from the wall layer and created a chaotically striated flow. The boundary layer grew due to merging of the large-scale structures and due to local entrainment of the dense material from the fluidized bed. The chaotic flow was averaged along similarity lines (i.e., lines of constant values of $x-r/R_s$ and $y=z/R_s$, where $R_s=ct$) to establish the main-flow profiles and the r.m.s fluctuating-flow profiles of the boundary layer. The profiles are qualitatively similar to our previous simulations of a dusty				
14. SUBJECT TERMS Surface-Burst Explosions Convective Mixing Simulations of Turbulent Flow bu- Dusty Boundary Layer Fluidized Bed			15. NUMBER OF PAGES 50	
			16. PRICE CODE	
17. SECURITY CLASSIFICATION OF REPORT UNCLASSIFIED	18. SECURITY CLASSIFICATION OF THIS PAGE UNCLASSIFIED	19. SECURITY CLASSIFICATION OF ABSTRACT UNCLASSIFIED	20. LIMITATION OF ABSTRACT SAR	

CLASSIFIED BY:

N/A since Unclassified.

DECLASSIFY ON:

N/A since Unclassified.

13. ABSTRACT (Continued)

boundary layer behind a planar shock. The boundary layer grew as a power function of distance behind the shock front:

$$\delta/R_s = 0.0256 \xi^{5/6}$$

where $\xi = 1 - x$. The exponent is similar to the value 4/5 reported for turbulent boundary layers on clean flat plates.

PREFACE

This work was sponsored by the Defense Nuclear Agency (DNA) under contract number DNA 001-88-C-0046 to Logicon RDA, and contract number MIPR-91-670 and MIPR-91-558 to the Naval Surface Warfare Center. The first author, Dr. Allen Kuhl, is a consultant to Logicon RDA and is an employee of the Lawrence Livermore National Laboratory (LLNL). Part of his work is performed under the auspices of the U.S. Department of Energy by LLNL under contract W-7405-ENG-48 and DNA IACRO number 91-853 and Work Unit 00354.

DTIC QUALITY INSPECTED 5

Accession For	
NTIS CRA&I	<input checked="" type="checkbox"/>
DTIC TAB	<input type="checkbox"/>
Unannounced	<input type="checkbox"/>
Justification	
By	
Distribution /	
Availability Codes	
Dist	Avail and/or Special
A-1	

CONVERSION TABLE

Conversion factors for U.S. customary to metric (SI) units of measurement

To Convert From	To	Multiply
angstrom	meters (m)	1.000 000 X E-10
atmosphere (normal)	kilo pascal (kPa)	1.013 25 X E+2
bar	kilo pascal (kPa)	1.000 000 X E+2
barn	meter ² (m ²)	1.000 000 X E-28
British Thermal unit (thermochemical)	joule (J)	1.054 350 X E+3
calorie (thermochemical)	joule (J)	4.184 000
cal (thermochemical)/cm ²	mega joule/m ² (MJ/m ²)	4.184 000 X E-2
curie	giga becquerel (GBq)*	3.700 000 X E+1
degree (angle)	radian (rad)	1.745 329 X E-2
degree Fahrenheit	degree kelvin (K)	$t_K = (t_F + 459.67)/1.8$
electron volt	joule (J)	1.602 19 X E-19
erg	joule (J)	1.000 000 X E-7
erg/second	watt (W)	1.000 000 X E-7
foot	meter (m)	3.048 000 X E-1
foot-pound-force	joule (J)	1.355 818
gallon (U.S. liquid)	meter ³ (m ³)	3.785 412 X E-3
inch	meter (m)	2.540 000 X E-2
jerk	joule (J)	1.000 000 X E+9
joule/kilogram (J/Kg) (radiation dose absorbed)	Gray (Gy)	1.000 000
kilotons	terajoules	4.183
kip (1000 lbf)	newton (N)	4.448 222 X E+3
kip/inch ² (ksi)	kilo pascal (kPa)	6.894 757 X E+3
kip	newton-second/m ² (N-s/m ²)	1.000 000 X E+2
micron	meter (m)	1.000 000 X E-6
mU	meter (m)	2.540 000 X E-5
mile (international)	meter (m)	1.609 344 X E+3
ounce	kilogram (kg)	2.834 952 X E-2
pound-force (lbf avoirdupois)	newton (N)	4.448 222
pound-force inch	newton-meter (N-m)	1.129 848 X E-1
pound-force/inch	newton/meter (N/m)	1.751 268 X E+2
pound-force/foot ²	kilo pascal (kPa)	4.768 026 X E-2
pound-force/inch ² (psi)	kilo pascal (kPa)	6.894 757
pound-mass (lbm avoirdupois)	kilogram (kg)	4.535 924 X E-1
pound-mass-foot ² (moment of inertia)	kilogram-meter ² (kg-m ²)	4.214 011 X E-2
pound-mass/foot ³	kilogram/meter ³ (kg/m ³)	1.601 846 X E+1
rad (radiation dose absorbed)	Gray (Gy)**	1.000 000 X E-2
roentgen	coulomb/kilogram (C/kg)	2.579 760 X E-4
shake	second (s)	1.000 000 X E-8
slug	kilogram (kg)	1.459 390 X E+1
torr (mm Hg, 0°C)	kilo pascal (kPa)	1.333 22 X E-1

*The becquerel (Bq) is the SI unit of radioactivity: Bq = 1 event/s.

**The Gray (Gy) is the SI unit of absorbed radiation.

TABLE OF CONTENTS

Section		Page
	PREFACE	iii
	CONVERSION TABLE	iv
	FIGURES	vi
1	INTRODUCTION	1
2	FORMULATION	5
3	RESULTS	7
	3.1 Flow Visualization	7
	3.2 Similarity Scaling	8
	3.3 Boundary Layer Growth	9
	3.4 Mean-Flow Profiles	12
	3.5 Fluctuating-Flow Profiles	13
4	DISCUSSION	14
5	CONCLUSION	16
6	REFERENCES	18
Appendix	MASS AND MOMENTUM INTEGRAL EQUATIONS FOR DUSTY BOUNDARY LAYERS	A-1

FIGURES

Figure		Page
1	Schematic of the calculation	21
2	Internal energy contours showing the shock interaction with the fluidized bed (FB) and the evolution of the wall boundary layer ($29 \text{ ms} \leq T \leq 451 \text{ ms}$).	22
3	Flowfield details near the shock front at $t = 451 \text{ ms}$: (a) density contours; (b) internal energy contours; (c) pressure contours; (d) vorticity contours; (e) entropy contours	24
4	Evolution of the freestream conditions above the boundary layer along lines of $x = \text{constant}$: (a) velocity; (b) density; (c) overpressure	25
5	Nondimensionalized flowfield for instantaneous freestream conditions $x = 0.7$, $z = 5, 205 \text{ cm}$: (a,a') streamwise velocity; (b,b') density; (c,c') pressure	26
6	Dusty boundary layer growth ANFO surface burst	27
7	Mean-flow boundary layer profiles ($0.7 \leq x \leq 0.9$): (a) streamwise velocity; (b) transverse velocity; (c) pressure; (d) density; (e) dynamic pressure	28
8	Mean-flow boundary layer profiles: (a) velocity; (b) specific volume; (c) dynamic pressure	29
9	R.M.S. fluctuation-flow profiles of the boundary layer ($0.7 \leq x \leq 0.9$): (a) streamwise velocity; (b) transverse velocity; (c) shear stress; (d) density; (e) pressure; (f) dynamic pressure	30
10	Local fluctuating-intensity profiles ($0.7 \leq x \leq 0.9$): (a) streamwise velocity; (b) transverse velocity; (c) density	31
11	Nondimensional mass entrainment rate \dot{M}_o versus distance x in an ANFO surface burst explosion ($\dot{M}_o = x \bar{\rho}_o \bar{v}_o / \rho_{co} u_{co}$).	32
12	Local mass scouring rate \dot{m}_o versus distance x in an ANFO surface burst. ($\dot{m}_o = \bar{\rho}_o \bar{v}_o / \rho_{co} U_{co}$)	32
A-1	Schematic of the turbulent dusty boundary layer induced by a shock (S) propagating along a loose dust bed (FB): (a) stationary coordinates; (b) similarity coordinates (ξ, y)	A-2

SECTION 1

INTRODUCTION

Turbulent, dusty boundary layers are an inherent feature of explosions over real ground surfaces. Detailed knowledge of dusty boundary layer characteristics is needed in explosion effects analysis. For example, to calculate the drag loads on above-ground structures, one needs to know the dusty boundary layer flow impinging on the structure. Also, to predict the amount of dust in the rising fireball of an explosion, one must know the dusty boundary layer swept up during the positive and negative phases of the blast wave and how much of this boundary layer dust is entrained into the stem of the dust cloud.

Turbulent dusty boundary layers differ dramatically from clean turbulent boundary layers. They are dominated by density effects which lead to baroclinically-generated vorticity ($\nabla p \times \nabla \rho$), in contrast with clean boundary layers which are dominated by viscous effects and wall drag. Dust densities near the wall are very large ($\rho_{\text{dust}}/\rho_{\text{air}} \gg 1$), and velocities are very small near the wall due to these density effects. Dusty boundary layers grow due to turbulent entrainment of dust from the wall, and this leads to much faster growth rates than in the clean case.

For explosion effects analysis, one would like to know the following properties of turbulent, dusty boundary layers: (1) the boundary layer thickness, because this scales the boundary layer profiles; (2) the mean-flow velocity and density profiles; (3) turbulent fluctuations in the boundary layer; and (4) the dust mass entrainment rate. Although considerable analytical and experimental studies have been performed, the aforementioned properties are not yet well established for turbulent dusty boundary layers in blast waves.

Initial investigations of nonsteady boundary layers utilized analytical methods such as the momentum integral equation, and were limited to clean, viscous flows. Typical examples are H. Mirels' classic solution of the turbulent boundary layer behind a normal shock,^{1,2} and the boundary layer induced by a self-similar hemispherical blast wave.^{3,4} More recently, Mirels⁵ and others⁶ have used similar analytical techniques to estimate the dust scouring induced by a shock wave, and to calculate

similarity solutions for turbulent dusty boundary layers (Frolov et al.⁷). Typically, the boundary layer profiles were assumed to be self-similar and obey a power-law function, hence the boundary flowfield was not actually calculated, as one does in hydrocode simulations.

Much of our fundamental understanding of turbulent dusty boundary layers comes from laboratory experiments. For example, B. Hartenbaum⁸ used a blowdown wind tunnel to measure the stagnation pressure profiles and dust scouring rate for a steady turbulent boundary layer over a loose dust bed. D. Ausherman⁹ used shock tube tests to study the mechanism of initial dust lofting induced by a normal shock. More recently, R. Batt¹⁰ has used a larger shock tube (with a test section of 17 in. high by 4 in. wide and an 18 ft-long dust bed) to study the turbulent boundary layer properties induced by a normal shock prepagating along a loose dust bed. He found that: (1) the velocity and density profiles could be approximated by a power-law function; (2) that the boundary layer grew approximately linearly with distance behind the shock; and (3) the dust scouring rate was 2 to 3 percent of the freestream mass flux. However, these experiments considered only the square-wave shock case, and are not directly applicable to blast wave problems.

Measurements were also made on large-scale field tests. These started with point explosions with typical yields of 10 to 20 KT, over a variety of ground surfaces (Glasstone¹¹). Stagnation pressure gauges were located at 3 and 10 ft elevation. The measurements were inadequate to establish the boundary layer profiles, and the mass scouring rate was not measured.

Next came blast wave field tests using HE sources. They began with studies of the clean turbulent boundary layer on 100 T-TNT surface burst test (MIDDLE GUST series). Carpenter¹² measured the stagnation pressure profiles at three ground ranges. This was followed by studies of the turbulent dusty boundary in a double-Mach-reflection flow (Pre-DIRECT COURSE Event; a 20-T ANFO sphere detonated at a HOB = 166 ft/KT^{1/3}). Stagnation pressure rakes were used to measure the stagnation pressure profiles of the dusty boundary layer¹³. Finally, the turbulent boundary layer in airblast precursor flows was investigated. Precursors were induced by a helium layer on the ground surface. These started with smaller-

scale tests in the DIAMOND ARC series (10^3 -lb HE detonated at HOB = 200 and 340 ft/KT^{1/3}). R. Reisler et al.¹⁴ used stagnation pressure rakes to measure the clean boundary layer profiles. Next came the Pre-MINOR SCALE Event which used a larger-scale charge (20-T ANFO surface burst). Hartenbaum¹⁵ used stagnation pressure rakes to measure stagnation pressure profiles on both the clean and dusty radials. These studies culminated in the MISTY PICTURE Event, employing a 4800-T ANFO hemisphere. Again, Hartenbaum¹⁶ used stagnation pressure rakes to investigate the boundary layer profiles on a dusty precursor flow. Nevertheless, a number of difficulties were encountered in these large-scale field tests. The primary difficulty was the accuracy of the stagnation pressure gauges to measure both the dust and air components of the flow. Second, the experimenters found it difficult to evaluate the mean-flow profiles from point measurements in the turbulent flow. Third, they found that it was impossible to measure the dust scouring rate in such nonsteady, turbulent flows. Hence, the laboratory-scale tests, along with hydrocode calculations, became the accepted approach.

As an alternative approach, hydrocode simulation techniques were developed. Typically they relied on a gasdynamics code to predict the evolution of the mean flow and a turbulence model to account for the mixing and transport of the dust. Such models have been used to simulate the dusty precursor flow on the MISTY PICTURE Event (Rosenblatt et al.¹⁷) and the clean precursor flow on the DIAMOND ARC tests (Needham et al.¹⁸). Such hydrocode simulations have met with only limited success — because the dust scouring rate function is not well established and because the turbulent transport rates are not known for dusty flows.

More recently, we have pursued a new approach — that is, a direct calculation of the turbulent mixing in the boundary layer flow by following the dynamic evolution of the rotational structures on the computational grid. This approach was used in numerical simulations of the turbulent dusty boundary induced by a normal shock,¹⁹ by a double-Mach-reflection shock structure,²⁰ by a self-similar precursor flow,²¹ and by shock reflections from wedges.²²

This paper applies this direct simulation approach to the blast wave case. The problem considered is the turbulent dusty boundary layer induced by an HE surface

burst explosion. The calculated flowfield was stored along similarity lines (i.e., lines of constant r/t^α and z/t^α). The solution was then time-averaged to evaluate the mean and fluctuating flow profiles in the boundary layer, and to establish the boundary layer thickness and dust entrainment rate. The next section presents the **Formulation** of the calculations. The **Results** section describes the rollup and mixing in the layer by flow visualization techniques, similarity scaling equations and empirical relations for the boundary layer growth, and the time-averaged profiles of the boundary layer. The **Discussion** section utilizes the Mass Integral Equation to interpret the results in the context of boundary layer theory. This is followed by a **Summary and Conclusions**.

SECTION 2 FORMULATION

A schematic of the problem is shown in Figure 1. The blast wave source was assumed to be a 570-T hemisphere of ANFO explosive ($R_c = 6.659$ m $\rho_c = 0.85$ g/cm³). This gives a blast wave that is equivalent to a 1-KT point explosion at low pressures. The blast wave propagated along a loose, fluid dust bed FB, creating a turbulent dusty boundary layer.

The analysis was based on the following idealizations: (1) the dust particles have a very small diameter, so the dust and air are in thermal and mechanical equilibrium; (2) the dust-air mixture behaves like a continuum fluid whose equation of state can be approximated by a dense-gas model; (3) the loose dust bed fluidizes immediately behind the shock; (4) the flow is two-dimensional (2-D); and (5) the fluid viscosity is zero (i.e., the dust density effects dominate the dynamics of the flow near the wall).

According to the preceding assumptions, the dynamics of the flow is governed by the 2-D inviscid conservation laws of gasdynamics:

$$\frac{\partial}{\partial t} \rho + \nabla \cdot (\rho \mathbf{u}) = 0 \quad (1)$$

$$\frac{\partial}{\partial t} \rho \mathbf{u} + \nabla (\rho \mathbf{u} \mathbf{u}) = - \nabla p \quad (2)$$

$$\frac{\partial}{\partial t} \rho E + \nabla \cdot (\rho E \mathbf{u}) = - \nabla \cdot (p \mathbf{u}) \quad (3)$$

where \mathbf{u} denotes the velocity and E represents the total energy: $E = e + 0.5 \mathbf{u} \cdot \mathbf{u}$. The pressure p is related to the density ρ and internal energy e by the equation of state:

$$p = (\gamma - 1) \rho e \quad (4)$$

where $\gamma(\rho, e)$ comes from a table lookup function for real air.²³ In the above, ρ actually represents the mixture density. The dust density ρ_d may be calculated from the relation:

$$\rho_d = \rho C \quad (5)$$

This requires an extra transport equation for the dust concentration C , namely:

$$\frac{\partial}{\partial t} C + (\mathbf{u} \cdot \nabla) C = 0 \quad (6)$$

These equations were integrated numerically by means of a high-order Godunov scheme for gasdynamics.²⁴

A $r - z$ cylindrical coordinates grid was used for the computational mesh. It consisted of a fine-mesh region ($100 \leq i \leq 600$ with an initial $\Delta r = 10$ cm; $1 \leq j \leq 100$ with an initial $\Delta z = 10$ cm) that followed the shock, and a stretched mesh region ($1 \leq i < 100$ with Δr variable) to capture the flow well behind the shock. The mesh was initialized with ambient air conditions (state 1):

$$p_1 = 1.01325 \times 10^6 \text{ dy/cm}^2; \rho_1 = 1.29 \times 10^{-3} \text{ g/cm}^3; \rho_d = 0;$$

$$C = 0; e_1 = 1.96 \times 10^9 \text{ erg/g}; \mathbf{u}_1 = 0; a_1 = 3.31 \times 10^4 \text{ cm/s.}$$

and a three-cell-thick fluidized dust bed (subscript FB):

$$p_{FB}/p_1 = 1; \rho_{FB}/\rho_1 = 38.67; \rho_d = 50 \times 10^{-3} \text{ g/cm}^3;$$

$$C = 0.9748; e_{FB}/e_1 = 0.0258; \mathbf{u}_{FB} = 0$$

at the bottom of the grid ($30\text{cm} \leq r \leq \infty; 0 \leq j \leq 3$). The flowfield inside the charge was initialized with the flowfield corresponding to an ideal Chapman-Jouguet detonation wave²⁵ with peak values of:

$$p_{cJ} = 60 \text{ Kbars } \rho_{cJ} = 1.262 \text{ g/cm}^3, \mathbf{u}_{cJ} = 1.518 \text{ km/s}, e_{cJ} = 4.976 \times 10^{10} \text{ erg/g}$$

for $R = \sqrt{r^2 + z^2} \leq R_c$ and $R_c = 6.659 \text{ m}$.

The left boundary of the mesh was treated as a symmetry condition. Wall drag was neglected at the bottom of the fluidized bed, hence an inviscid slip boundary condition ($v = 0, \partial u/\partial z = 0, \partial p/\partial z = 0$) was used at the bottom boundary. The top and right boundaries of the mesh were treated as outflow conditions.

The calculation was run for 5000 computational cycles, and the results were stored along similarity lines for later statistical analysis. This required about 10 cpu hours on the Cray XMP computer. The results are described in the next section.

SECTION 3 RESULTS

3.1 FLOW VISUALIZATION.

Figure 2 depicts a sequence of frames of internal energy contours that show the evolution of the flow from early times (29 ms) to late times (451 ms). The first frame shows the incident shock I as well as the contact surface CS (denoting the outer boundary of the detonation products DP) and the backward-facing shock I' that are inherent features of HE-driven blast waves. The incident shock I compresses the fluidized bed FB and deposits vorticity at the top of the layer by the baroclinic mechanism: $\nabla p \times \nabla \rho$. The layer is unstable and rolls up into a turbulent mixing layer, i.e., a turbulent boundary layer BL . The boundary layer grows in height with increasing distance behind the shock front.

Figure 2 also shows that the flow field interacts with the leading edge of the fluidized bed (initially located at $r = 30$ m), forming a bow shock BS . The bow shock then interacts with the contact surface of the fireball, creating vorticity which rolls up into a large rotational structure RS . The vorticity field created by this interaction causes dense material from the leading edge region LE to become entrained up into the fireball. This entrainment process influences (i.e., pollutes) the natural growth of the boundary layer underneath the fireball ($0 \leq r \leq 100$ m).

Figure 3 presents contour plots that show some of the boundary layer details near the shock front at $t = 451$ m. The vorticity contours demonstrate that vorticity is indeed generated by the interaction of the incident shock I with the top of the fluidized bed. This shear layer is unstable and rolls up into a turbulent boundary layer. The density, internal energy and entropy contours make visible the rotational structures and mixing processes in the boundary layer BL .

3.2 SIMILARITY SCALING.

For surface burst explosions, there are only two characteristic length scales in the problem: (1) the shock front radius $R_s(t)$, and (2) the thickness of the fluidized bed z_{FB} . If we consider explosions that are large compared to the fluidized bed thickness (i.e., $R_s/z_{FB} \rightarrow \infty$), then only a single characteristic length scale remains, namely, R_s . For strong explosions, the shock front trajectory satisfies a power-law relation:

$$R_s = ct^\alpha \quad (7)$$

where $\alpha = 2/5$ for point explosions and $\alpha \simeq 0.54$ for HE-driven blast waves. Under such circumstances, the blast wave flowfield is self-similar,²⁶ and the number of independent variables may be reduced from three (r, z, t) to two $(r/t^\alpha, z/t^\alpha)$, namely:

$$x = r/R_s \quad (8)$$

$$y = z/R_s \quad (9)$$

In these coordinates, the blast wave flow field above the boundary layer (denoted by subscript ∞) is self-similar and independent of time in the strong shock regime, i.e.,

$$u_\infty/u_2 = F(x) \quad (10)$$

$$p_\infty/p_2 = G(x) \quad (11)$$

$$\rho_\infty/\rho_2 = H(x) \quad (12)$$

where subscript 2 denotes the state behind the shock. In these coordinates, the laminar solution will remain constant. They thus provide an ideal tool for analyzing the fluctuating flow of the turbulent boundary layer. Hence, each timestep the flow field was sampled along similarity lines:

$$x = 0.1, 0.2, 0.3, 0.4, 0.5, 0.6, 0.7, 0.75, 0.8, 0.85, 0.9$$

$$0 < y \leq 0.04$$

and stored for statistical analysis.

Figure 4, depicts the calculated flowfield evolution above the boundary layer (i.e., at $z = 15.4$ m) that was sampled along similarity lines $x = 0.7, 0.8$ and 0.9 . The blast wave flowfield decays as a function of time. The curves are reasonably smooth but small oscillations, caused by acoustic radiation from the turbulent fluctuations in the boundary layer, are evident.

The flowfield was nondimensionalized by the instantaneous freestream conditions, i.e.,

$$u(x, z, t)/u_{\infty}(x, t)$$

$$\rho(x, z, t)/\rho_{\infty}(x, t)$$

$$p(x, z, t)/p_{\infty}(x, t)$$

and plotted as a function of time. Figure 5 presents a typical example of such results for $x = 0.7$. It shows that the streamwise velocities at the bottom of the fluidized bed ($z = 5$ cm) oscillate near a zero value, while the velocities near the top of the boundary layer $z = 205$ cm oscillate around a value of one. Densities at the bottom of the fluidized bed oscillate around value of $\rho_{\infty} \simeq 30$, and return to a value of one at the top of the boundary layer. Pressures remain essentially constant throughout the layer. These results suggest a blast wave scaling for the boundary layer:

$$\bar{u}/u_{\infty} = f(x, y) \tag{13}$$

$$\bar{p}/p_{\infty} = g(x, y) \tag{14}$$

$$\bar{\rho}/\rho_{\infty} = h(x, y) \tag{15}$$

where the bar denotes an appropriate time-averaging operation. The functions f, g , and h then represent the mean boundary layer profiles. Of course, one of the main objectives of this study is to calculate these boundary layer profiles.

3.3 BOUNDARY LAYER GROWTH.

Let us define the top of the boundary layer as the height y_{BL} where the mean streamwise velocity \bar{u} reaches ninety-nine percent of its freestream value (i.e., y_{BL} equals the y where $\bar{u}/u_{\infty} = 0.99$). And let us define the bottom of the boundary

layer as the mean top of the fluidized bed y_{FB} (i.e., the height where these Reynolds stresses go to zero and where the density profiles converge). Then the boundary layer thickness δ becomes:

$$\delta/R_s = y_{BL} - y_{FB} \quad (16)$$

The boundary layer thickness evaluated from the numerical simulation is presented in Figure 6. This figure shows that the boundary layer grows as a power-law function of the distance behind the shock:

$$\delta/R_s = 0.0256 \xi^{5/6} \quad (17)$$

where

$$\xi = 1 - x \quad (18)$$

This power-law is similar to that found for the turbulent boundary layer growth on a clean flat plate $\delta \sim (\Delta r)^{4/5}$, however, the growth mechanisms are different. Clean boundary layers grow because of local wall drag, while dusty boundary layers grow because of turbulent entrainment of dust from the fluidized bed.

Table 1 presents a comparison of boundary layer growth for other self-similar turbulent dusty boundary layer problems. The numerical simulation technique was the same one that was used for the present results. This table shows that for a variety of self-similar problems, the turbulent dusty boundary layer grows as a power-law function of ξ :

$$\delta/R_s = a\xi^\beta \quad (19)$$

For decaying blast wave problems, the exponent is $\beta = 5/6$; while for square-wave shock reflections from dusty wedges, the exponent is typically $\beta = 3/5$. Apparently not only the exponent β , but the constant a are not universal but depend on the problem details. In other words, the mass entrainment rate (which feeds the boundary layer growth) depends on local pressure gradients, separated flow effects, wall jet effects, etc.

Table 1. Boundary layer growth.

CASE	BOUNDARY LAYER GROWTH	β
Clean Flat Plate ¹⁸	$\delta/\chi = 0.37 Re_\chi^{-1/5}$ $\delta \sim \chi^{4/5}$	4/5
<u>SQUARE WAVE SHOCK REFLECTIONS</u> ²²		
Normal Shock - Case 1 ($M_I = 1.7, \theta_w = 0^\circ$)	$\delta/R_s = 0.037 \xi^{3/5} (0 < \xi < 0.7)$	3/5
RR - Case 2 ($M_I = 2, \theta_w = 60^\circ$)	$\delta/R_s = 0.0157 \xi^{3/5} (0 < \xi < 0.6)$	3/5
SMR - Case 3 ($M_I = 2, \theta_w = 27^\circ$)	$\delta/R_s = 0.0147 \xi^{3/5} (0 < \xi < 0.3)$	3/5
DMR - Case 4 ($M_I = 10, \theta_w = 30^\circ$)	$\delta/R_s = f_1(\xi)$ $\simeq 0.0213 \xi^{3/5} (0 < \xi < 0.25)$	3/5
Precursor Case ¹⁷ ($M_I = 1.7, \rho_{TL}/\rho_1 = 0.1, \rho_{FB}/\rho_1 = 50$)	$\delta/R_J = f_2(\xi)$ $\simeq 0.0325 \xi^{5/6}$	5/6
Normal Shock, infinitely-long fluidized bed ¹³ ($M_I = 1.7, \rho_{FB}/\rho_1 = 50$)	$\delta/R_s = 0.024 \xi$	1

<u>SHOCK TUBE EXPERIMENTS</u>		
Normal shock over loose soil bed ⁹ ($M_I = 1.7$)	$\delta_t = 0.0325(\Delta\chi)^{5/6}$ [χ] = cm δ_t = tangent slope thickness	5/6
Normal shock along a clean wall ⁹ ($M_I = 1.7$)	$\delta_t = 0.00983(\Delta\chi)^{0.93}$	0.93
<u>DECAYING BLAST WAVES</u>		
ANFO Surface Burst over loose dust bed ($20 \leq \Delta p_I(\text{psi}) \leq 80, \rho_{FB}/\rho_1 = 50$)	$\delta/R_s = 0.0256 \xi^{5/6}$	5/6
Point Explosion Surface Burst over loose dust bed ($1000 \leq \Delta p_I(\text{psi}) \leq 8000, \rho_{FB}/\rho_1 = 50$)	$\delta/R_s = 0.086 \xi^{5/6}$	5/6
HOB=50 ft/KT ^{1/3} over deep snow ($3 \leq \Delta p_I(\text{kb}) \leq 10, \rho_{FB}/\rho_1 = 200$)	$\delta_v/\xi R_s = 0.0886 \xi^{5/6}$ $\delta_v/\xi R_s = 0.110 \xi^{5/6}$	5/6 5/6

$\delta = z$ where $\bar{u} = 0.99 U_\infty$
 δ_t = tangent slope thickness

3.4 MEAN-FLOW PROFILES.

The flow field variables ϕ were time-averaged along similarity lines to establish the mean-flow profiles:

$$\bar{\phi}(x, y) = \int \phi(x, y, t) dt / \tau \quad (20)$$

where $\phi = (u/u_{\infty}, \rho/\rho_{\infty}, p/p_{\infty}, \text{etc})$. The integration duration τ was taken as $200 \text{ ms} \leq t \leq 451 \text{ ms}$; this allowed time for the boundary layer to develop before starting the averaging and stopped the averaging before the effects of the negative phase influenced the solution. The profiles were then scaled with the boundary layer thickness, i.e.:

$$\eta = \frac{y - y_{\text{FB}}}{(\delta/R_s)} \quad (21)$$

Note that the boundary layer region of the flow corresponds to the domain $0 < \eta \leq 1$, while the region of $\eta < 0$ corresponds to the flow field inside the fluidized bed.

The mean-flow profiles of the boundary layer are presented in Figure 7. Using the boundary layer scaling (Eq. 21), the mean streamwise velocity and density profiles collapse to similarity profiles $\bar{u}/u_{\infty} = f(\eta)$ and $\bar{\rho}/\rho_{\infty} = h(\eta)$ that are independent of distance (for $0.7 \leq x \leq 0.9$). The vertical velocities were small but positive ($\bar{v}/u_{\infty} = 0.02$) at the bottom of the layer, due to net mass entrainment from the fluidized bed. They increased to a value of above 0.04 to 0.12 at the top of the boundary layer in order to accommodate the divergence of the hemispherical blast wave. The mean static pressures remained constant throughout the layer. The dynamic pressures overshoot within the layer (i.e., $\bar{q}/q_{\infty} > 1$) at larger distances behind the shock, perhaps due to nonsteady effects.

Figure 8 presents some of the same profiles in semi-log coordinates which allow one to investigate the details near the bottom of the layer. This figure shows that the present velocities profiles are similar to our previous calculation of a dusty boundary layer behind a normal shock (labeled DG3), and similar to the laser-doppler-velocimetry measurements of dusty boundary layers in shock tubes (Batt et al.¹⁰). Velocities are essentially zero near the bottom of the layer ($0 \leq \eta \leq 0.1$) because of the large values of density near the fluidized bed. The specific volume

($\lambda = 1/\rho$) profiles are somewhat steeper than the DG3 calculation and the x-ray measurements,¹⁰ perhaps due to nonsteady effects.

3.5 FLUCTUATING-FLOW PROFILES.

The r.m.s. fluctuations were calculated from the relation:

$$\phi'(x, y) = \left[\int \{ \phi(x, y, t) - \bar{\phi}(x, y) \}^2 dt / \tau \right]^{1/2} \quad (22)$$

The fluctuating-flow profiles of the boundary layer are presented in Figure 9. Streamwise velocity fluctuations peak at a value of about $u'/u_\infty = 0.25$, similar to other turbulent boundary layers. Vertical velocity fluctuations increase with distance behind the shock, and reach a value about $v'/u_\infty = 0.2$ at $x = 0.75$. Perhaps this is a blast wave effect, because the Reynolds stresses also increase with distance behind the shock. They reach a value of $\overline{u'v'}/u_\infty^2 = -80 \times 10^{-3}$. The density fluctuations reached a peak value of about seven times the freestream value because of turbulent entrainment of dense material from the fluidized bed. Static pressure fluctuations were small ($p'/p_\infty = 0.05$ to 0.10). Dynamic pressure fluctuations, however, were quite large ($q' \sim q_\infty$) and increased with distance behind the shock.

Figure 10 depicts the local fluctuating-intensity profiles of the dusty boundary layer. The local fluctuations are very large: $u'/\bar{u} \simeq 1$ to 10 , $v'/\bar{v} \simeq 5$ and $\rho'/\bar{\rho} \simeq 1$ in the layer. This flow is considerably different from clean turbulent boundary layers, where turbulent intensities are limited to 10 to 20 percent. Apparently the turbulent fluctuations dominate the mean flow in turbulent dusty boundary layers.

SECTION 4 DISCUSSION

This section explores the mechanisms of the growth of the wall layer in the context of boundary layer theory. We start by defining the mass thickness δ_m , which is related to the boundary layer thickness δ according to:

$$\delta_m = I_m \delta \quad (23)$$

Here I_m represents the integral of the mass and mass-flux profiles taken over the boundary layer:

$$I_m = \left(\frac{\gamma + 1}{2} \frac{x}{F(x)} - 1 \right) \int_0^1 (h - 1) d\eta + \int_0^1 h(1 - f) d\eta \quad (24)$$

If the density and velocity profiles are self-similar (i.e., $h = h(\eta)$ and $f = f(\eta)$), then the mass integral becomes a simple function of x . For example, evaluating the above integrals by using the self-similar profiles from Figure 7, one finds

$$\begin{aligned} I_m(x) &= (1.2x/F(x) - 1)1.004 + 1.035 \\ &= 1.2x/F(x) + 0.03 \end{aligned} \quad (25)$$

Next, consider the boundary layer Mass Integral Equation

$$\frac{d}{d\xi} [xH(x)F(x)I_m(x)\delta/R_s] = \dot{M}_o - x\rho_{\infty}v_{\infty}/\rho_2u_2 \quad (26)$$

which may be derived from a control volume analysis of the mass flux in the boundary layer. In the above, \dot{M}_o represents the nondimensional rate that mass is being entrained into the bottom of the boundary layer due to turbulent mixing:

$$\dot{M}_o = x \overline{\rho_o v_o} / \rho_2 u_2 \quad (27)$$

Thus, the Mass Integral Equation (Eq. 26) states that the fundamental reason that dusty boundary layer grows is because of turbulent mass entrainment from the fluidized bed (i.e., because of \dot{M}_o). Note that this is true independent of momentum considerations.

The nondimensional mass entrainment rate was evaluated from the numerical simulation. The result is presented in Figure 11, which shows that the entrainment rate started at a value of $0.035 \rho_2 u_2$ at the shock front, and decayed with distance behind the shock. Near the front, the entrainment rate may be approximated by the equation:

$$\begin{aligned} \dot{M}_o &= -0.065 + 0.1x \\ &= 0.035 - 0.1\xi \end{aligned} \quad (28)$$

which represents the straight line curve in Figure 11.

In other hydrocode simulations,¹⁷ dust mass is injected into the bottom row of cells in the mesh according to the so-called local mass scouring rate \dot{m}_o , defined as:

$$\dot{m}_o = \overline{\rho_o v_o} / \rho_{\infty} u_{\infty} \quad (29)$$

This parameter was also evaluated from our calculational results, and is presented in Figure 12. This figure shows that the scouring rate starts with a value $\dot{m}_o = 0.035$ at the shock front, but rapidly increases with distance behind the shock. This happens not because the mass entrainment rate increases dramatically, but because both ρ_{∞} and u_{∞} which were used in the nondimensionalization become smaller at increasing distances from the shock front.

Such comparisons demonstrate that the mass entrainment rate for strong blast waves is most properly scaled with the shock front values of ρ_2 and u_2 (i.e., according to Eq. 27), and not with the local conditions of ρ_{∞} and u_{∞} . Such scaling follows naturally from the Mass Integral Equation for blast waves.

SECTION 5 CONCLUSIONS

Interactions between the incident shock front and the dense fluidized bed generated vorticity near the wall by the baroclinic mechanism: $\nabla p \times \nabla \rho$. The resulting wall shear layer was unstable, and rolled up into large-scale rotational structures which formed a turbulent mixing layer near the wall — that is, a numerically-simulated turbulent boundary layer.

The boundary layer grew due to merging of vortex structures and due to entrainment of dense material from the fluidized bed. Analysis of the calculation showed that the dusty blast wave boundary layer grew as a power function of distance behind the shock:

$$\delta/R_s = 0.0256 \xi^{5/6}$$

This growth is qualitatively similar to the growth that was observed in our previous calculations²² of turbulent boundary layers created by shock reflections from dusty wedges: $\delta/R_s = a \xi^{3/5}$ where $0.015 \leq a \leq 0.037$. Apparently the dusty boundary layer growth function is not universal but is problem-dependent (e.g., the growth is influenced by pressure gradients, local flow features, etc.).

By using the Mass Integral Equation, it was demonstrated that the fundamental cause of dusty boundary layer growth was mass entrainment from the fluidized bed. For this blast wave case, the mass entrainment rate decayed linearly with distance behind the shock

$$\dot{M}_o = \pi \overline{\rho_o v_o} / \rho_2 u_2 = 0.035 - 0.1\xi$$

The mean-flow velocity and density profiles were qualitatively similar to the measured profiles for a normal shock propagating along a loose dust bed. The peak values of the r.m.s. fluctuations were qualitatively similar to those found in turbulent boundary layers. Nevertheless, experimental data on dusty blast wave boundary layers are needed to quantitatively check the accuracy of these calculations.

The numerical simulations described here provide a useful tool for studying mixing layers that are dominated by the evolution of baroclinically-generated vorticity,

such as dusty boundary layers. This method should be used to calculate turbulent mixing in a variety of non-self-similar blast wave problems.

SECTION 6 REFERENCES

1. Mirels, H. "Boundary Layer Behind a Shock or Thin Expansion wave Moving into a Stationary Fluid," National Advisory Committee for Aeronautics, Wash., D.C., TN-3712, 1956.
2. Mirels, H. "The Wall Boundary Layer behind a Moving Shock wave," in Boundary underbarLayer Research, Proceedings of the International Union of Theoretical and Applied Mechanics, edited by H. Görtler, Springer-Verlag, Berlin, 1958, pp. 283-293.
3. Mirels, H. and Hamman, J. "Laminar Boundary Layer behind a Strong Shock Moving with Nonuniform Velocity," Physics of Fluids, Vol. 5(1), 1962, pp. 91-96.
4. Crawford, D.R., Quan, V., and Ohrenberger, J.T., Blast Wave Turbulent Boundary Layers, DNA-2768F, 1972.
5. Mirels, H. "Blowing Model for Turbulent Boundary-Layer Dust Ingestion," AIAA Journal, Vol. 22(11), 1984, pp. 1582-1589.
6. M.R. and Baum, E., Dusty Boundary Layer Modeling, DNA-001-84-C-0107, 1984.
7. Frolov, S.M., Mack, A. and Roth, P. "Diffusion Model of Dust Lifting Behind a Shock," Thirteenth Int. Colloq. on Explosions and Reactive Systems, 1991 (in press).
8. Hartenbaum, B., Lofting of Particles by a High-Speed Wind, DNA-2737, 1974.
9. Ausherman, D. Initial Dust Lofting: Shock Tube Experiments, DNA-31-62F, Wash., D.C., 1973.
10. Batt, R.G., Kulkarny, V.A., Behrens, H.W., Rungaldier, H., "Shock-Induced Boundary Layer Dust Lofting," Shock Tubes and Waves, edited by H. Grönig, VCH, Weinheim, Germany, 1988, 209-215.
11. Glasstone, S. The Effects of Nuclear Weapons, U.S. Atomic Energy Commission, 1962.
12. Carpenter, H.J., Hove, D., Batt, R.G., and Dillinger, B., "Blast Wave Boundary Layer Measurements," AFWL-TR-73-211, 1974.

13. Hartenbaum, B., DIRECT COURSE measurements (private communication).
14. Reisler, R. et al., DIAMOND ARC measurements (private communication).
15. Hartenbaum, B., Pre-MINOR SCALE measurements (private communication).
16. Hartenbaum, B., "Dusty Airblast Gas Dynamic (Snob/Greg) Measurements," Proceedings of the MISTY PICTURE Symposium, Vol. 7, Ch. 9, POR-7187-7, Defense Nuclear Agency, Alexandria, VA, 1990.
17. Rosenblatt, M., "Comparisons of a Preshot Calculation to MISTY PICTURE Dusty Precursed Airblast Data," Proceedings of the MISTY PICTURE Symposium, Vol. 7, Ch. 11, Defense Nuclear Agency, Alexandria, VA, 1990.
18. Needham, C., DIAMOND ARC calculations (private communication).
19. Kuhl, A.L., Chien, K.-Y., Ferguson, R.E., Collins, J.P., Glaz, H.M. and Colella, P., "Simulation of a Turbulent Dusty Boundary Layer Behind a Shock," Current Topics in Shock Waves, edited by Y.W. Kim, American Institute of Physics Press, New York, 1990, pp. 762-769.
20. Kuhl, A.L., Ferguson, R.E., Chien, K.-Y., Glowacki, W., Collins, J.P., Glaz, H. and Colella, P., "Turbulent Wall Jet in a Mach Reflection Flow," Dynamics of Detonations and Explosions: Explosion Phenomena, Progress in Astronautics and Aeronautics 134, edited by A.L. Kuhl, J.-C. Leyer, A.A. Borisov, W.A. Siriginano, AIAA, Wash., D.C., 1991, pp. 201-232.
21. Kuhl, A.L., Glowacki, W., Chien, K.-Y., Ferguson, R.E., Collins, J.P., Glaz, H.M., and Colella, P. "Simulation of a Turbulent Wall Jet in a Precursor Flow," Proceedings of the Eleventh International Symposium on Military Applications of Blast Simulation, edited by A. Mark of Ballistics Research Laboratories, 1989.
22. Kuhl, A.L., Ferguson, R.E., Chien, K.-Y., and Collins, P. "Unstable Wall Layers Created by Shock Reflections from Wedges," Thirteenth Int. Colloq. on Dynamics of Explosions and Reactive Systems, 1991, (in press).
23. Gilmore, F. "Equilibrium Composition and Thermodynamic Properties of Air to 24,000 K," RM-1543, Rand Corp., Santa Monica, CA, 1955.

24. Colella, P. and Glaz, H.M., "Efficient Solution Algorithms for the Riemann Problem for Real Gases," Journal of Computational Physics, Vol. 59(2), 1985, pp. 264-289.
25. Taylor, G.I. "The Dynamics of Combustion Products Behind Plane and Spherical Detonation Fronts in Explosives," Proc. Royal Society, A 200, 1950, pp. 235-247.
26. Sedov, L.I., Similarity and Dimensional Methods in Mechanics, Academic Press, New York, 1959.
27. Schlichting, H. Boundary Layer Theory, McGraw Hill, New York, 1968.

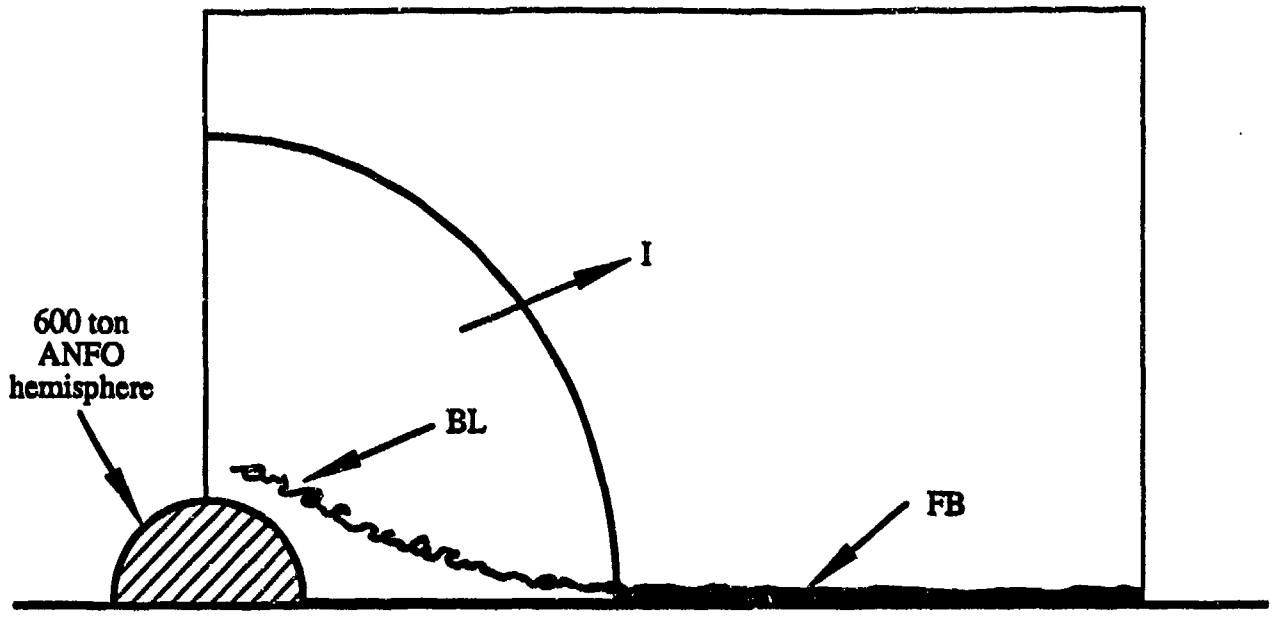


Figure 1. Schematic of the calculation.

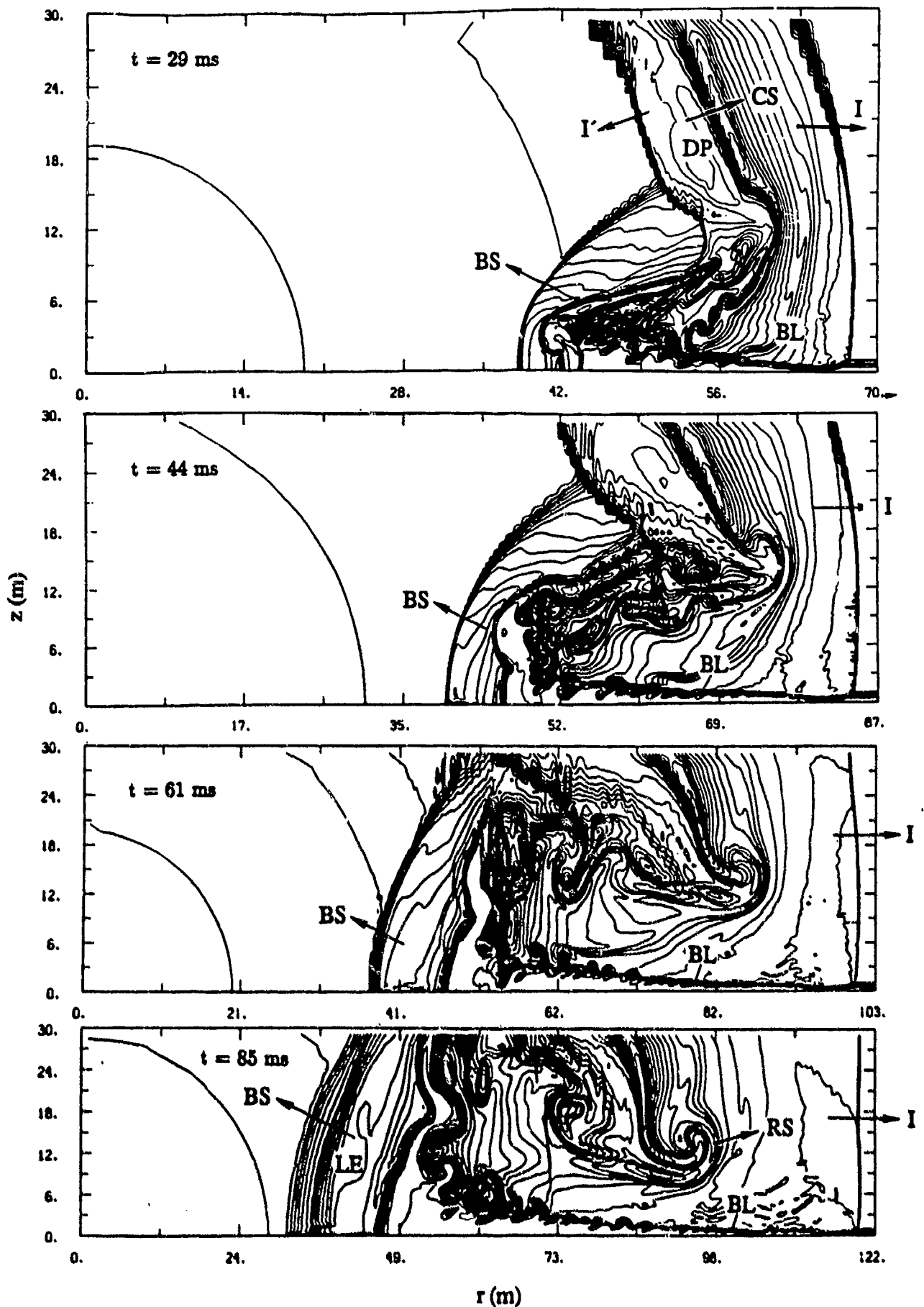


Figure 2. Internal energy contours showing the shock interaction with the fluidized bed (FB) and the evolution of the wall boundary layer ($29 \text{ ms} \leq T \leq 451 \text{ ms}$).

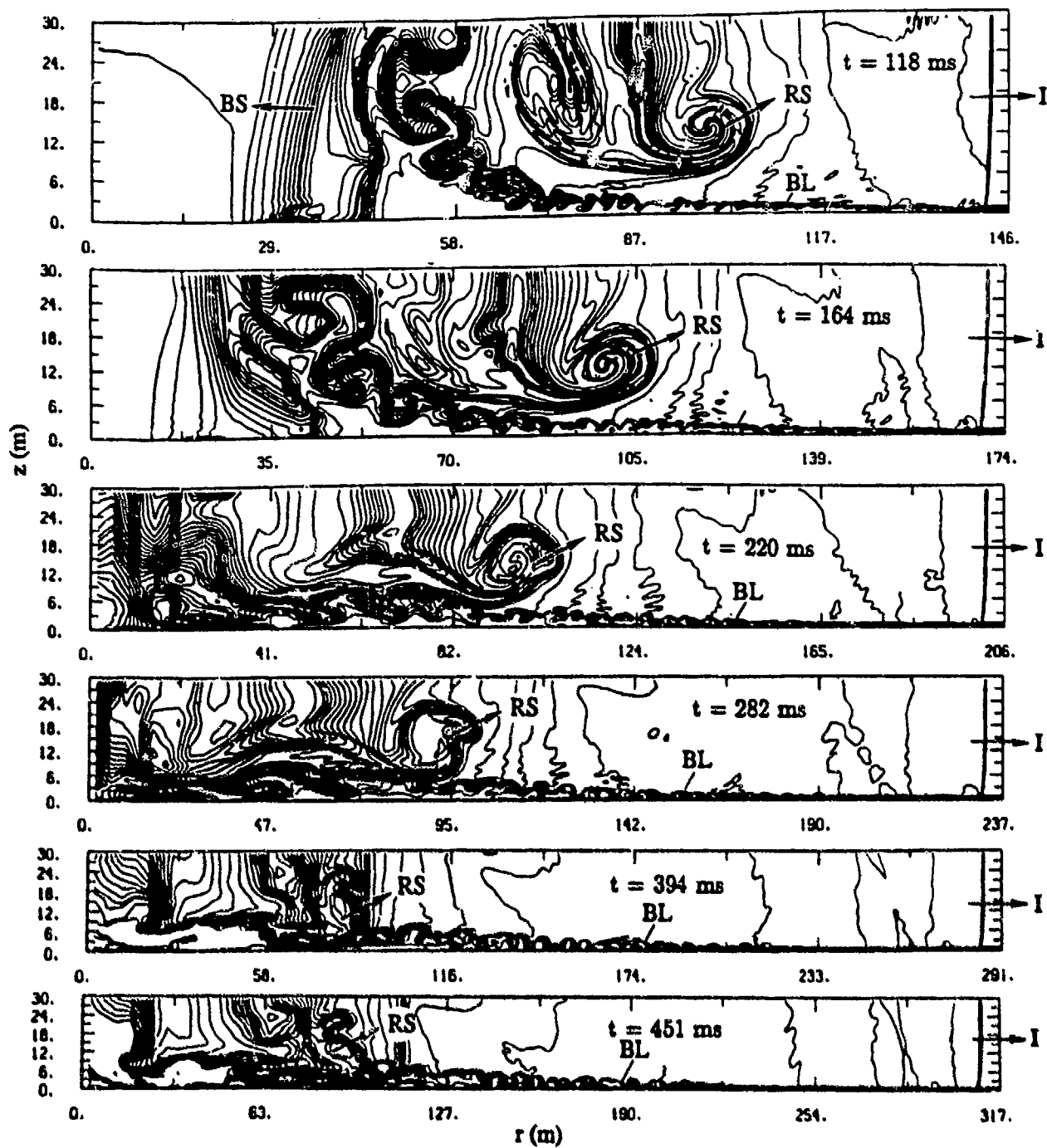


Figure 2. Internal energy contours showing the shock interaction with the fluidized bed (FB) and the evolution of the wall boundary layer ($29 \text{ ms} \leq T \leq 451 \text{ ms}$) (Continued).

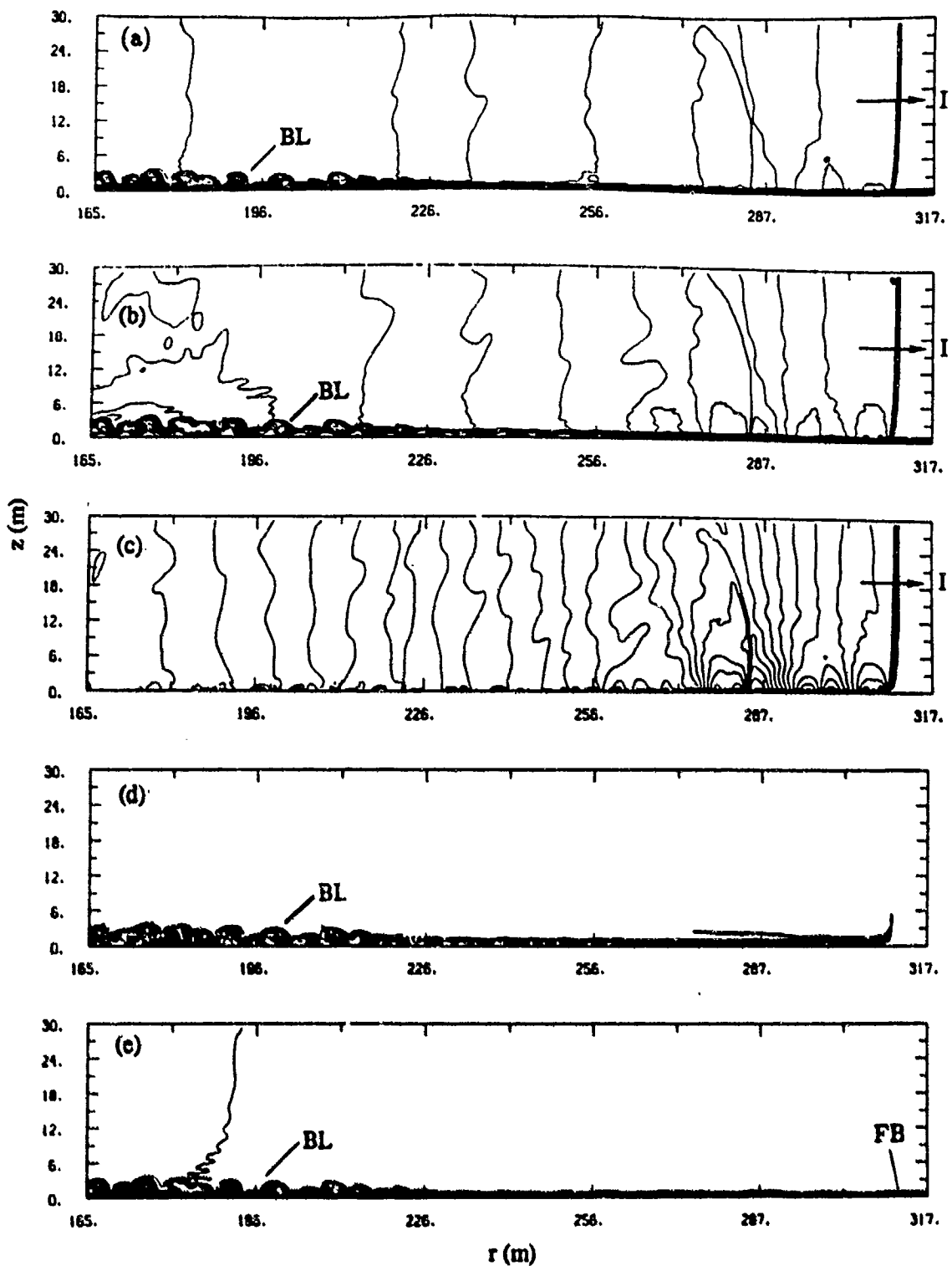


Figure 3. Flowfield details near the shock front at $t = 451$ ms: (a) density contours; (b) internal energy contours; (c) pressure contours; (d) vorticity contours; (e) entropy contours.

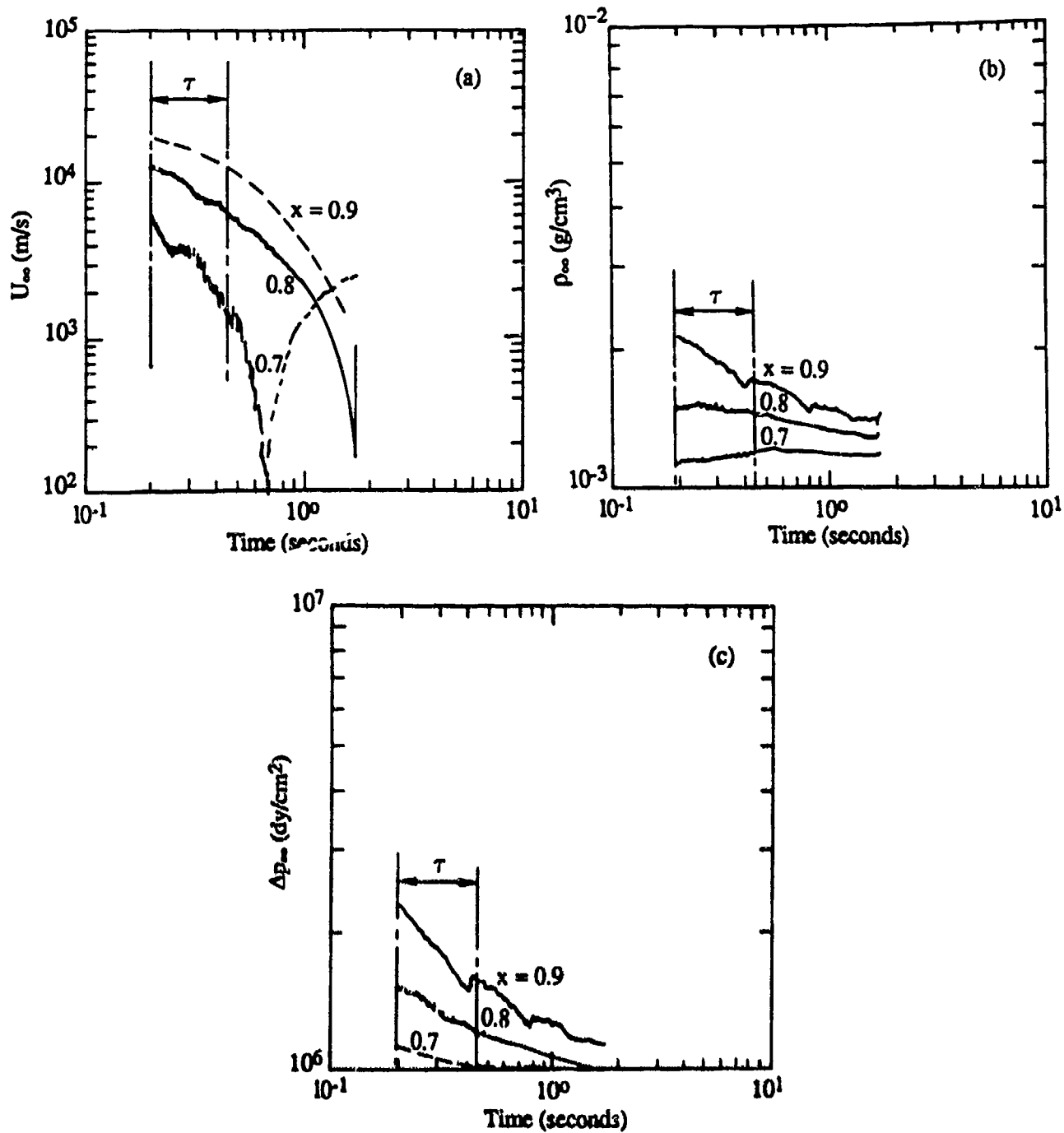


Figure 4. Evolution of the freestream conditions above the boundary layer along lines of $x = \text{constant}$: (a) velocity; (b) density; (c) overpressure.

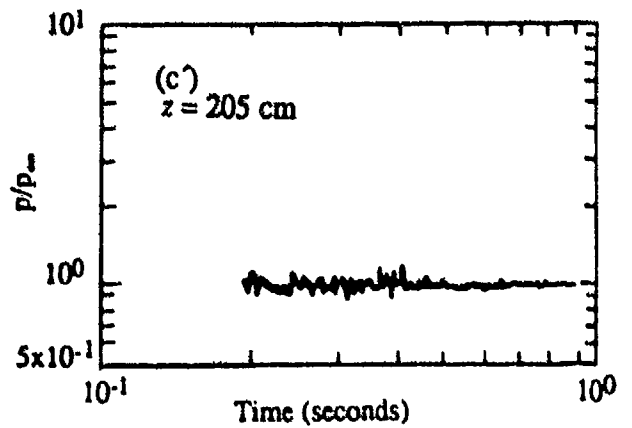
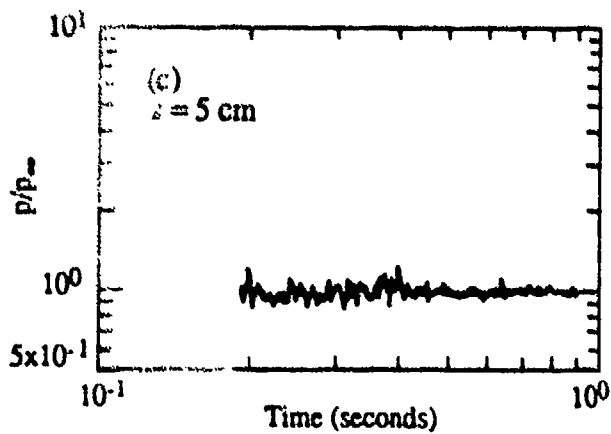
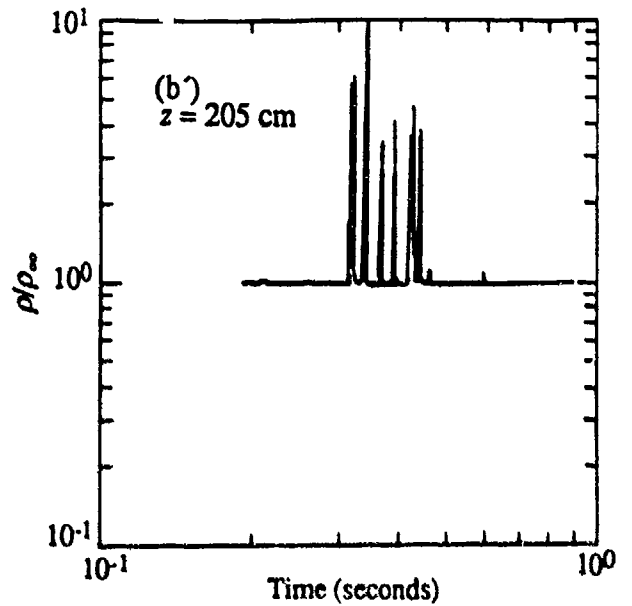
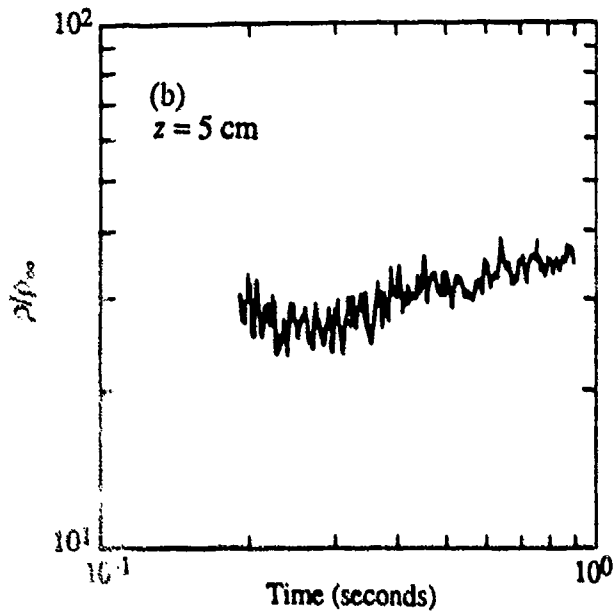
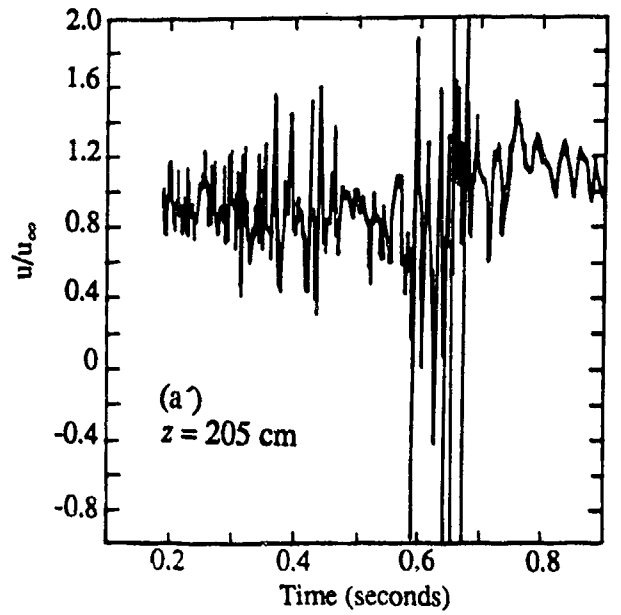
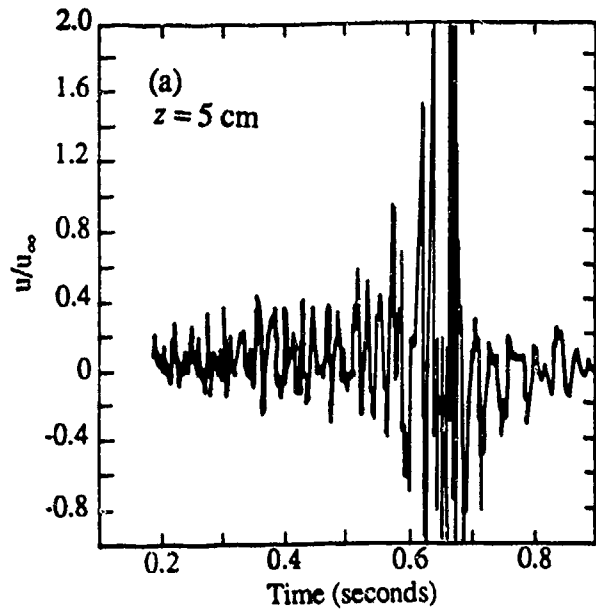


Figure 3. Nondimensionalized flowfield for instantaneous freestream conditions $x = 0.7$, $z = 5, 205 \text{ cm}$: (a, a') streamwise velocity; (b, b') density; (c, c') pressure.

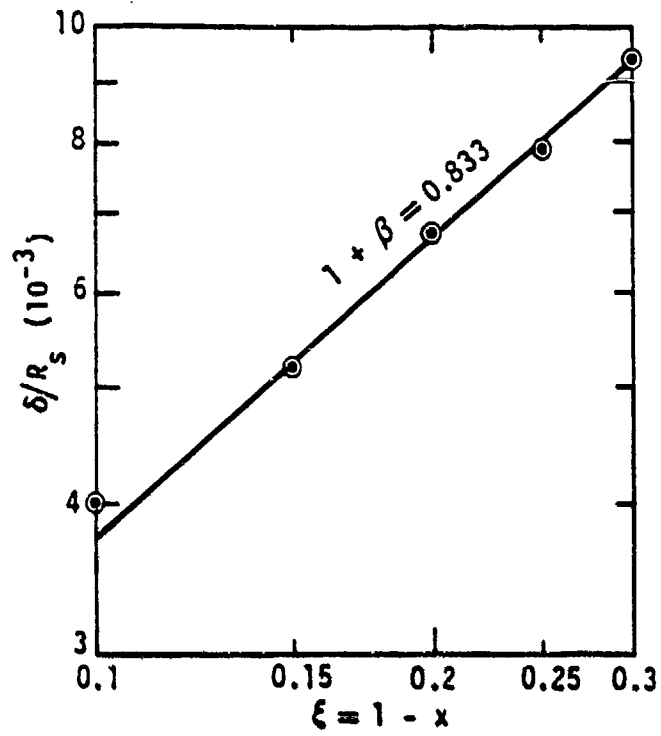


Figure 6. Dusty boundary layer growth ANFO surface burst.

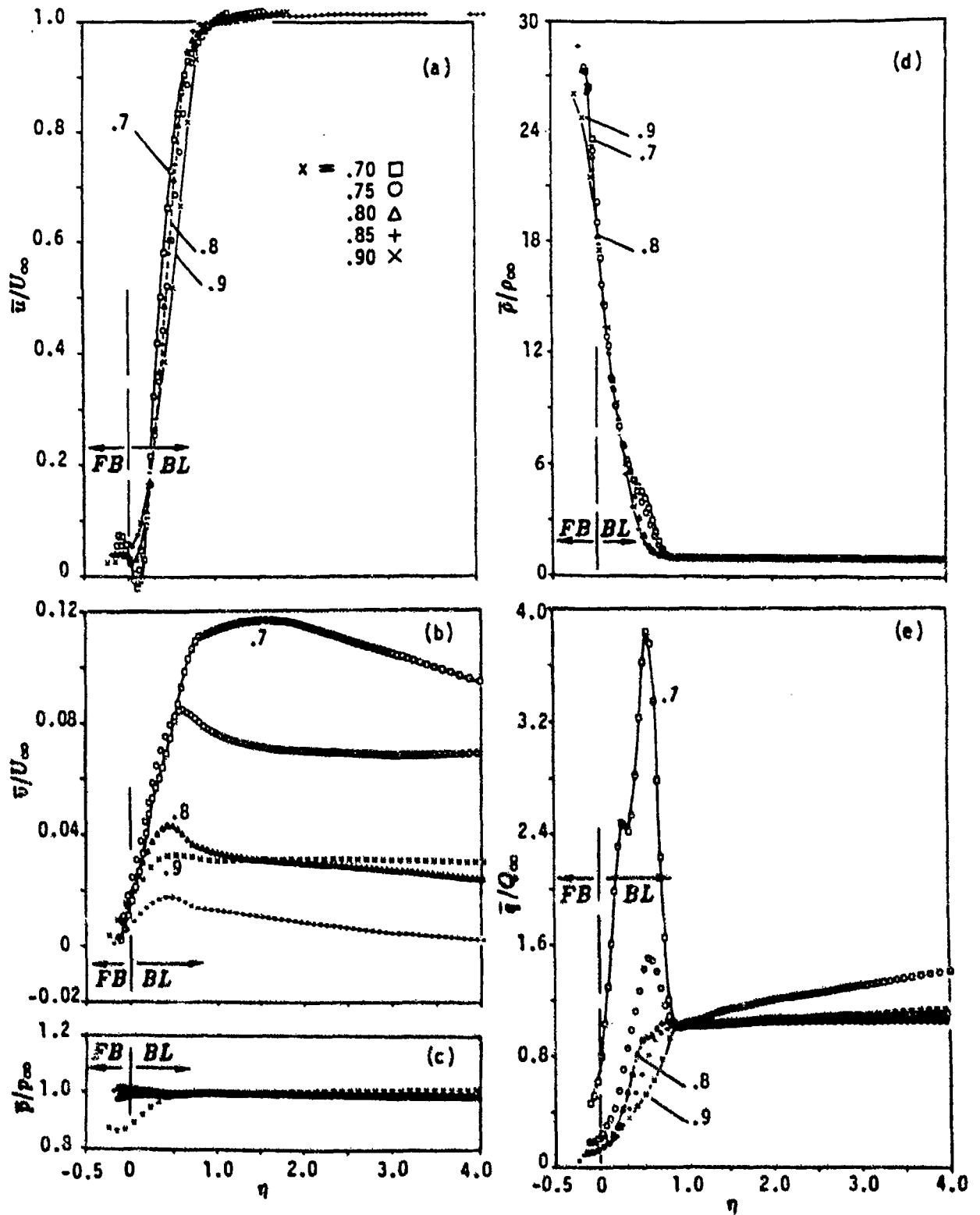


Figure 7. Mean-flow boundary layer profiles ($0.7 \leq x \leq 0.9$): (a) streamwise velocity; (b) transverse velocity; (c) pressure; (d) density; (e) dynamic pressure.

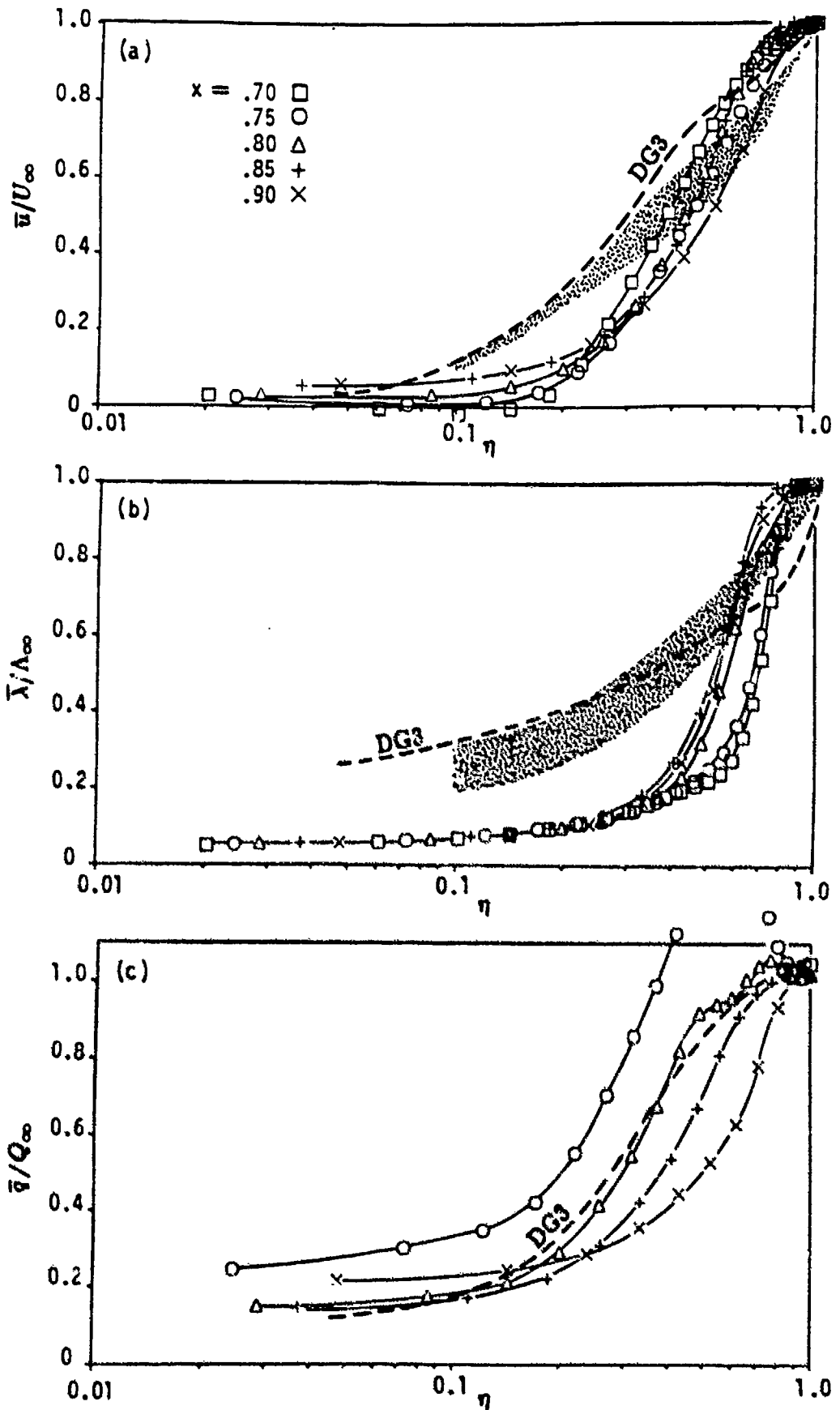


Figure 8. Mean-flow boundary layer profiles: (a) velocity; (b) specific volume; (c) dynamic pressure. Shaded regions denote data bands of Batt et al., (1988). The dashed DG3 lines are for $x = 950$.

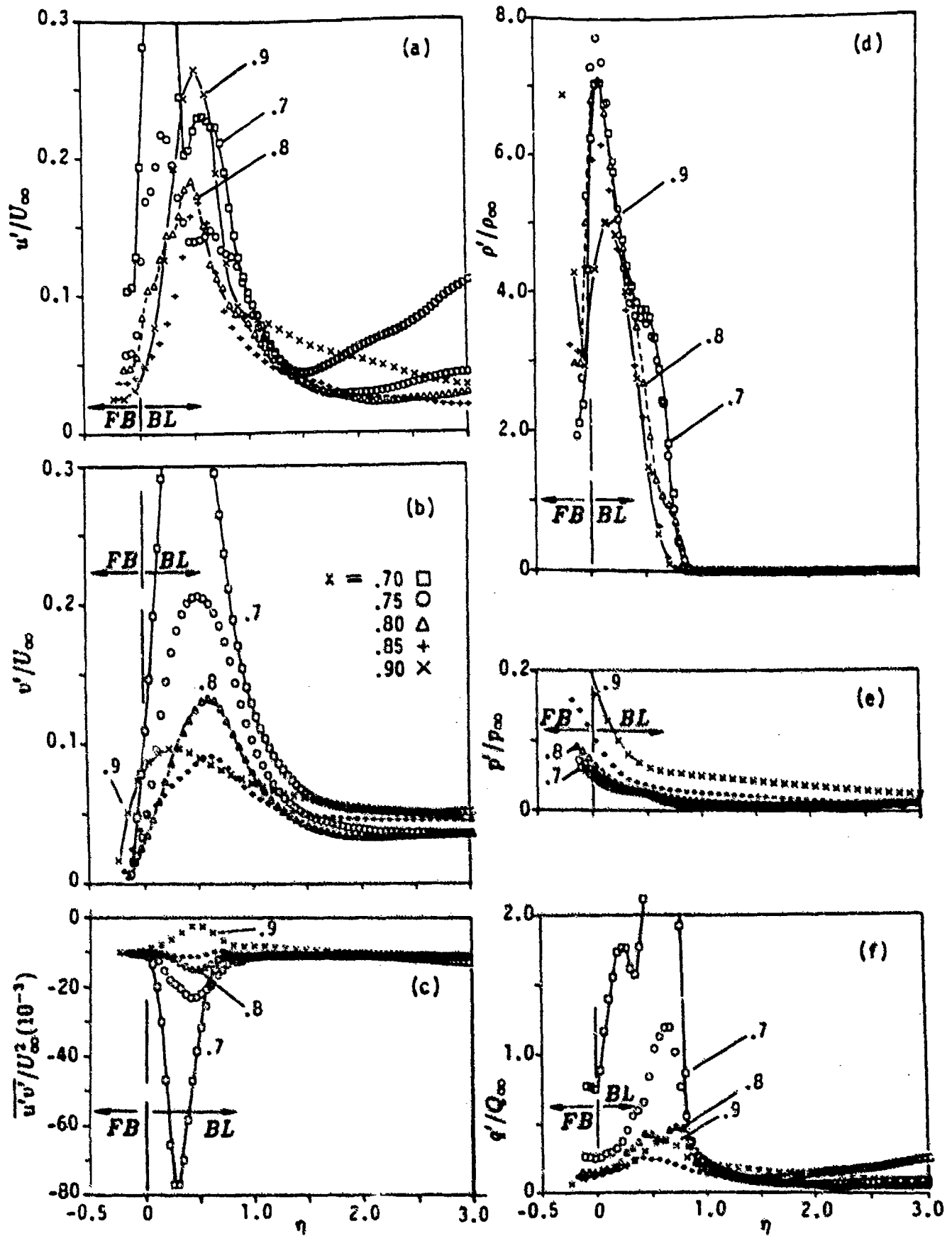


Figure 9. R.M.S. fluctuating-flow profiles of the boundary layer ($0.7 \leq x \leq 0.9$):
 (a) streamwise velocity; (b) transverse velocity; (c) shear stress; (d) density;
 (e) pressure; (f) dynamic pressure.

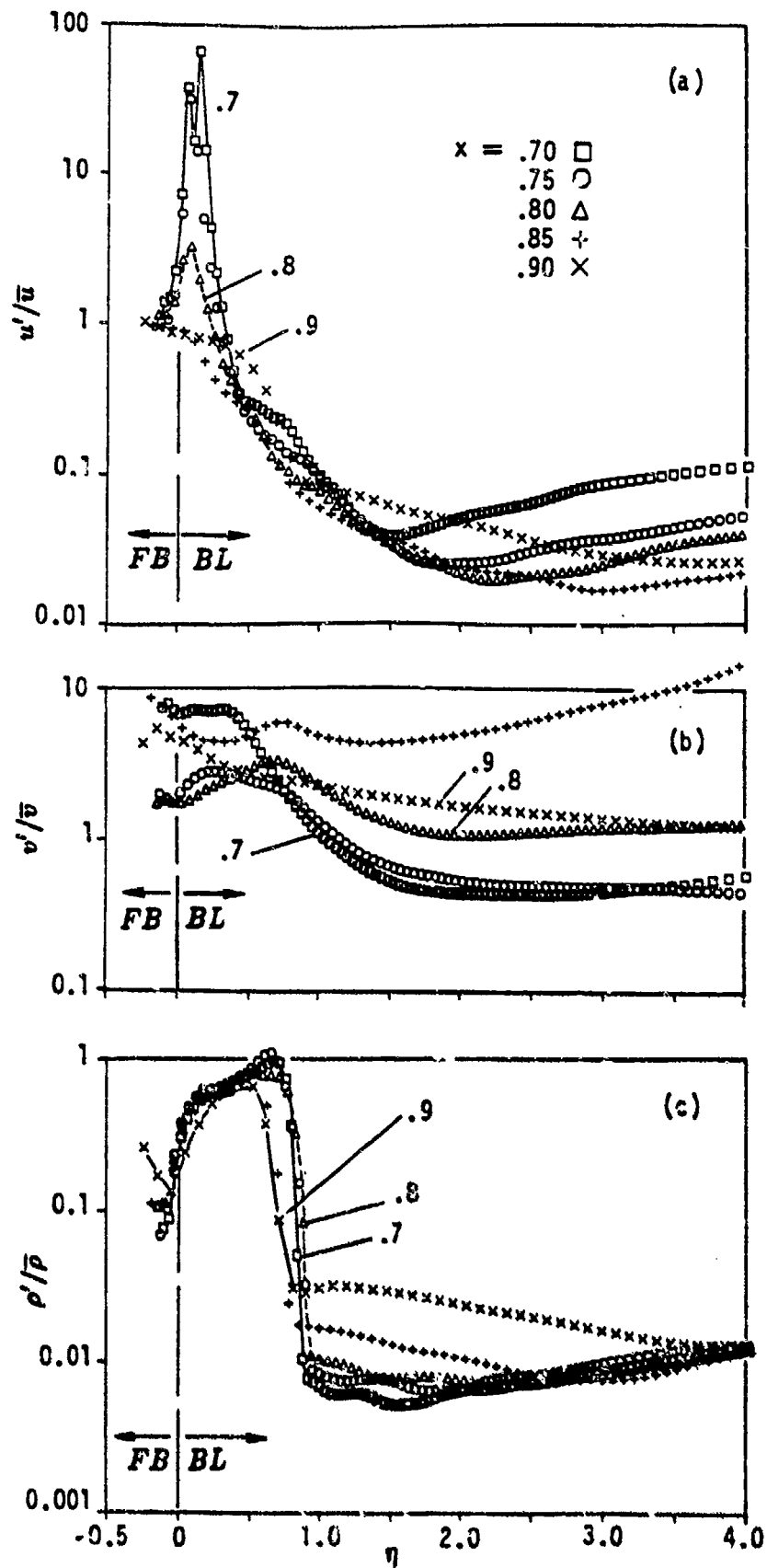


Figure 10. Local fluctuating-intensity profiles ($0.7 \leq x \leq 0.9$):
 (a) streamwise velocity; (b) transverse velocity;
 (c) density.

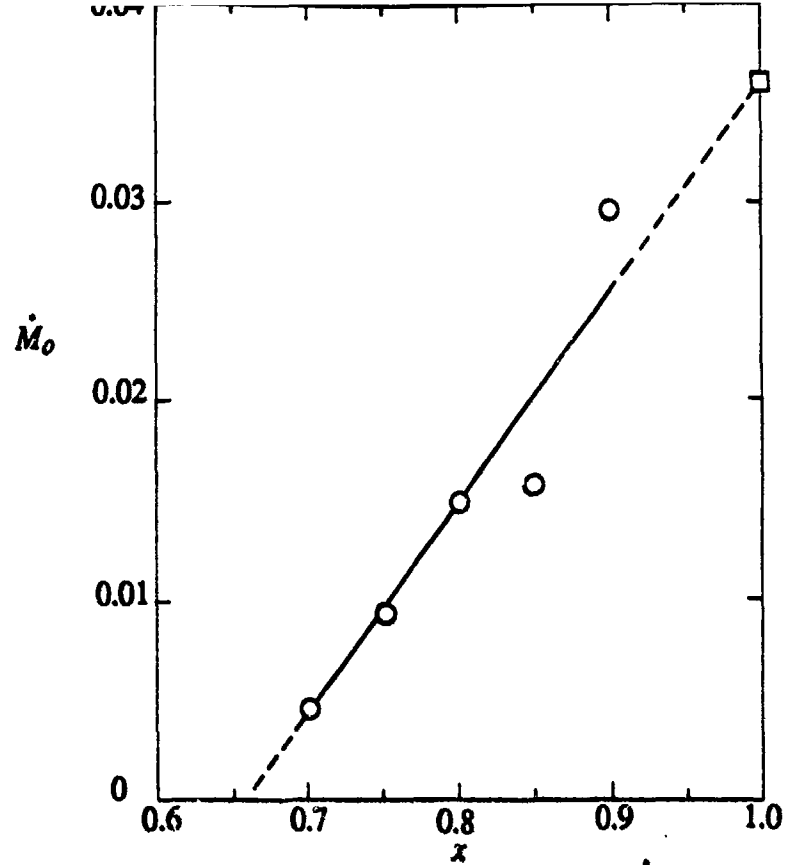


Figure 11. Nondimensional mass entrainment rate \dot{M}_0 versus distance x in an ANFO surface burst explosion ($\dot{M}_0 = x\bar{\rho}_0\bar{V}_0/\rho_2u_2$).

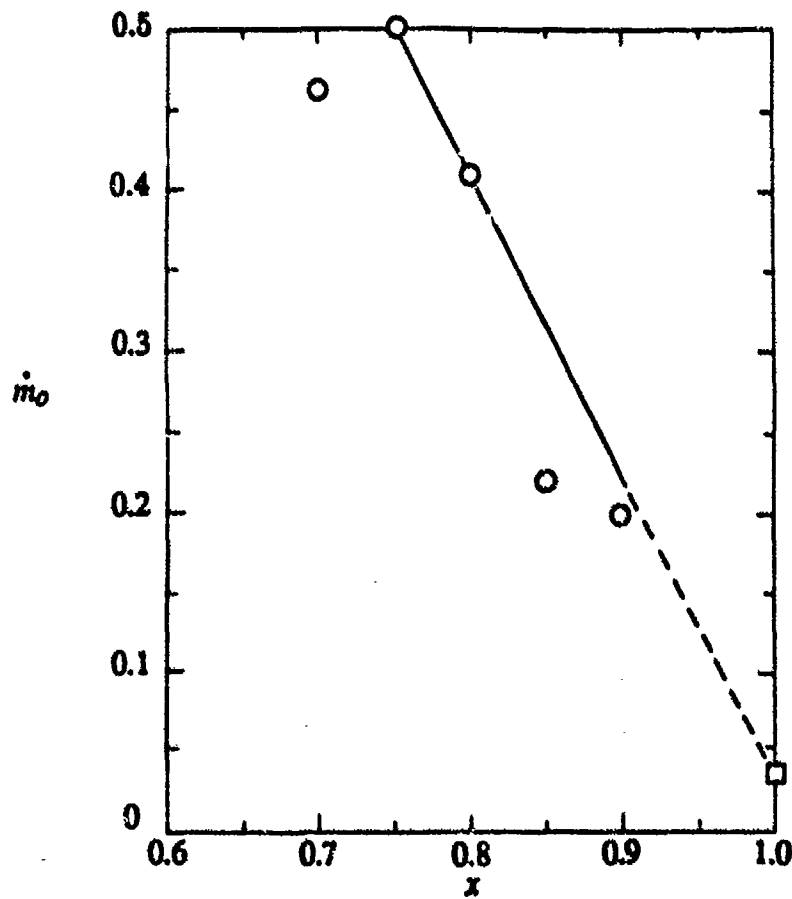


Figure 12. Local mass scouring rate \dot{m}_0 versus distance x in an ANFO surface burst ($\dot{m}_0 = \bar{\rho}_0\bar{V}_0/\rho_wU_w$).

APPENDIX
MASS AND MOMENTUM INTEGRAL EQUATIONS
FOR DUSTY BOUNDARY LAYERS

Described here is an analysis of the turbulent dusty boundary layer created by a shock wave that is propagating along a loose dust bed. The problem is depicted in Figure A-1. In stationary coordinates (Fig. A-1a), the shock wave S propagates with a velocity W_s ; states ahead and behind the shock are denoted by subscript 1 and 2, respectively. Flow interactions with the fluidized bed FB, create a velocity deficit (shown as the shaded regions D_a and D_b) in the mean streamwise velocity profiles. Densities increase near the wall due to entrainment of dust from the fluidized bed. The boundary layer grows because of turbulent entrainment of dust.

To analyze the flow, we define the following similarity coordinates. First, assume that the shock front propagates as a power-law function of time:

$$R_s(t) = ct^\alpha \quad (\text{A1})$$

where $\alpha = 2/5$ for point-explosions, $\alpha \simeq 0.54$ for HE explosions and $\alpha = 1$ for square waves. In such cases, the shock-induced flow field above the boundary layer is constant along lines of

$$x = r/R_s = 1 - \xi \quad (\text{A2})$$

$$y = z/R_s \quad (\text{A3})$$

These similarity lines propagate with a wave velocity

$$W = xW_s \quad (\text{A4})$$

The streamwise velocity in these similarity coordinates becomes:

$$\tilde{u} = W - u = xW_s - u \quad (\text{A5})$$

This transformation modifies the velocity profiles as depicted in Figure A-1b. In this case, the velocity begins with the freestream value $\tilde{u}_\infty = xW_s - u_\infty$ at the edge of the boundary layer, and increases to a maximum value of $\tilde{u}_W = xW_s$ on the wall.

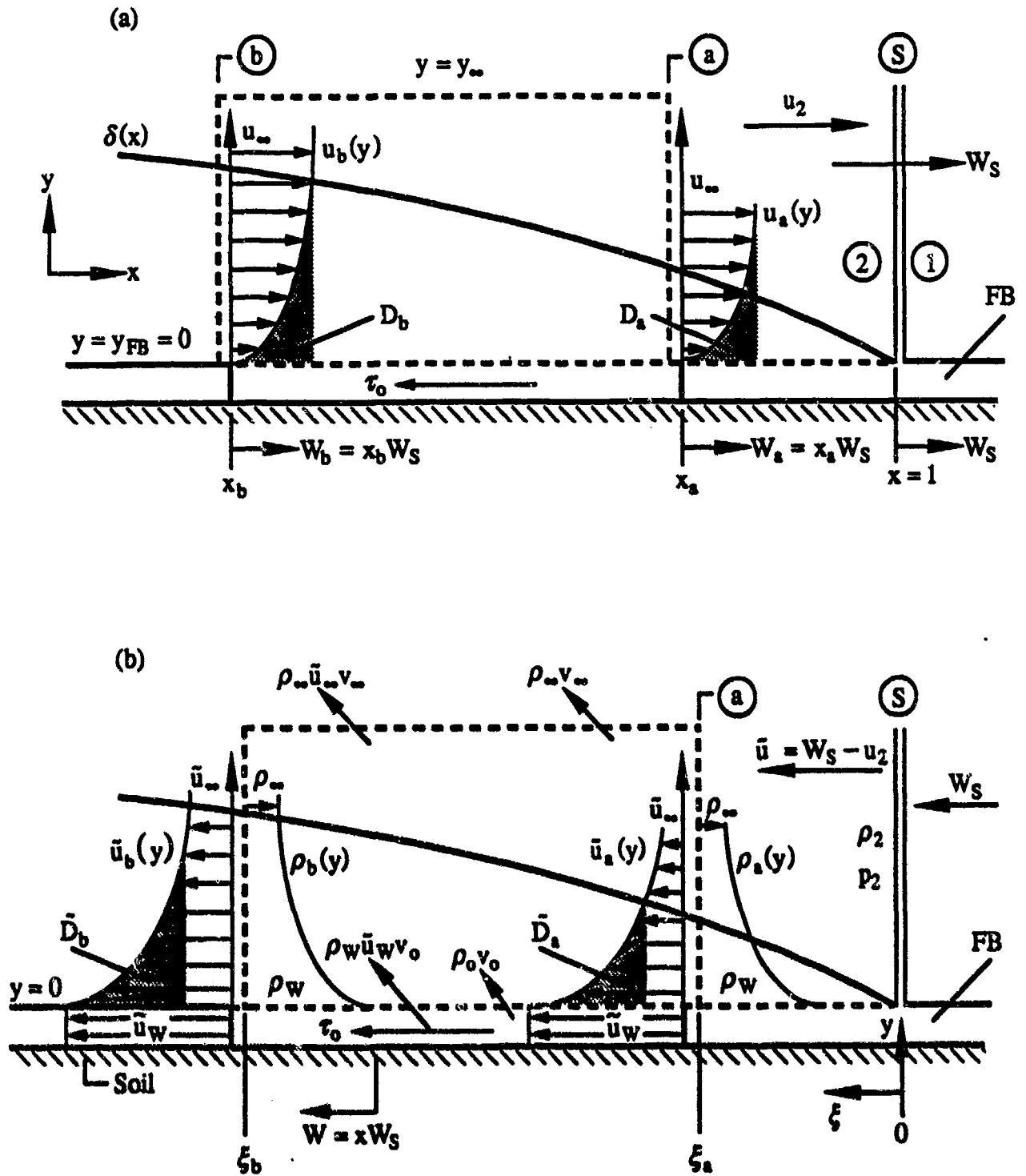


Figure A-1. Schematic of the turbulent dusty boundary layer induced by a shock (S) propagating along a loose dust bed (FB):
 (a) stationary coordinates; (b) similarity coordinates (ξ, y).

Described here is a control volume analysis of the mass and momentum balance for such turbulent boundary layers, assuming that the mean velocity and density profiles, $f = u/u_\infty$ and $h = \rho/\rho_\infty$, are known.

A.1 MASS INTEGRAL EQUATION.

Let \tilde{F}_i represent the mass flux across surface i of the control volume in the similarity coordinates of Figure A1-b. Then the streamwise fluxes across the cylindrical surfaces a and b (surface area $2\pi x dy$) are given by:

$$\begin{aligned}\tilde{F}_a &= 2\pi x_a \int_0^{y_\infty} \rho_a \tilde{u}_a dy \\ &= 2\pi x_a (\delta_a/R_s) \int_0^1 \rho_a \tilde{u}_a d\eta + 2\pi x_a \rho_\infty \tilde{u}_\infty (y_\infty - \delta_a/R_s)\end{aligned}\quad (A6)$$

$$\begin{aligned}\tilde{F}_b &= 2\pi x_b \int_0^{y_\infty} \rho_b \tilde{u}_b dy \\ &= 2\pi x_b (\delta_b/R_s) \int_0^1 \rho_b \tilde{u}_b d\eta + 2\pi x_b \rho_\infty \tilde{u}_\infty (y_\infty - \delta_b/R_s)\end{aligned}\quad (A7)$$

Similarly, the mass fluxes through the bottom and top of the control volume are:

$$\tilde{F}_o = 2\pi x \rho_o v_o \Delta x \quad (A8)$$

$$\tilde{F}_\infty = 2\pi x \rho_\infty v_\infty \Delta x \quad (A9)$$

Since the flow is steady in these similarity coordinates, then the conservation of mass requires that the sum of the fluxes is equal to zero:

$$\sum_i \tilde{F}_i = 0$$

or

$$\tilde{F}_a - \tilde{F}_b + \tilde{F}_o - \tilde{F}_\infty = 0 \quad (A10)$$

Solving the above equation for the streamwise flux yields:

$$(\tilde{F}_a - \tilde{F}_b)/\Delta x = 2\pi x (-\rho_o v_o + \rho_\infty v_\infty) \quad (A11)$$

Taking the limit as Δx approaches zero and using $d\xi = -dx$, we find the mass conservation law:

$$\frac{d}{d\xi} \tilde{F}_m = x \rho_o v_o - x \rho_\infty v_\infty \quad (A12)$$

where

$$\begin{aligned}\tilde{F}_m &= x(\delta/R_s) \left[\int_0^1 \rho \tilde{u} d\eta - \rho_\infty \tilde{u}_\infty \right] \\ &= x(\delta/R_s) \int_0^1 (\rho \tilde{u} - \rho_\infty \tilde{u}_\infty) d\eta\end{aligned}\quad (\text{A13})$$

The latter represents the surplus mass flux (relative to the freestream values) created by the wall boundary layer. The mass conservation law (Eq. A12) can be nondimensionalized by the mass flux $\rho_2 u_2$, yielding:

$$\frac{d}{d\xi} [xHF \delta_m/R_s] = \dot{m}_o - xHF v_\infty/u_\infty \quad (\text{14})$$

where

$$\dot{m}_o = x\rho_o v_o/\rho_2 u_2 \quad (\text{A15})$$

$$H(x) = \rho_\infty/\rho_2 \quad (\text{A16})$$

$$F(x) = u_\infty/u_2 \quad (\text{A17})$$

In the above, \dot{m}_o represents the nondimensional mass entrainment rate, and $H(x)$ and $F(x)$ denote the nondimensional flow field above the boundary layer which can be a function of x . In addition, δ_m represents the mass thickness of the boundary layer:

$$\delta_m = \delta \int_0^1 (h\tilde{f} - \tilde{f}_\infty) d\eta \quad (\text{A18})$$

where

$$h(x, \eta) = \rho/\rho_\infty \quad (\text{A19})$$

$$\tilde{f}(x, \eta) = \tilde{u}/u_\infty = xW_s/u_\infty - f \quad (\text{A20})$$

$$\tilde{f}_\infty(x) = xW_s/u_\infty - f_\infty \quad (\text{A21})$$

$$f(x, \eta) = u/u_\infty \quad (\text{A22})$$

Next, we convert the above integrand to lab-fixed velocity profiles ($f = u/u_\infty$):

$$\begin{aligned}h\tilde{f} - \tilde{f}_\infty &= h[xW_s/u_\infty - f] - xW_s/u_\infty + 1 \\ &= \frac{W_s}{u_2} \frac{x}{F(x)} (h - 1) + (1 - hf)\end{aligned}\quad (\text{A23})$$

The expression for the boundary layer mass thickness then simplifies to:

$$\delta_m = I_m \delta \quad (\text{A24})$$

where

$$I_m(x) = \frac{W_s}{u_2} \frac{x}{F(x)} \int_0^1 (h-1) d\eta + \int_0^1 (1-hf) d\eta \quad (\text{A25})$$

Using the above relations, the Mass Integral Equation becomes:

$$\frac{d}{d\xi} [xHF I_m \delta / R_s] = \dot{m}_o - xHF v_\infty / u_\infty \quad (\text{A26})$$

This equation may be integrated to determine the boundary layer growth as a function of ξ :

$$\delta(\xi) / R_s = \int_0^\xi (\dot{m}_o - HF v_\infty / u_\infty) d\xi / HFI_m \quad (\text{A27})$$

Thus, mass conservation in the boundary proves that the fundamental cause of dusty boundary layer growth is mass entrainment from the fluidized bed. Note that this is true independent of momentum considerations (e.g., for zero wall drag).

If the freestream conditions are independent of x (e.g., in the normal shock case), then the above relations reduce to a particularly simple form:

$$\frac{d}{d\xi} [I_m \delta / R_s] = \dot{m}_o - v_\infty / u_\infty \quad (\text{A28})$$

and

$$\delta(\xi) / R_s = \int_0^\xi (\dot{m}_o - v_\infty / u_\infty) d\xi / I_m \quad (\text{A29})$$

A.2 MOMENTUM INTEGRAL EQUATION.

Now let \bar{F}_i represent the momentum flux across surface i of the control volume in similarity coordinates. Then the streamwise fluxes across cylindrical surfaces a and b are given by:

$$\begin{aligned} \bar{F}_a &= 2\pi x_a \int_0^{y_\infty} \rho_a \bar{u}_a^2 dy + 2\pi x_a \int_0^{y_\infty} p_a dy \\ &= 2\pi x_a \left[(\delta_a / R_s) \int_0^1 \rho_a \bar{u}_a^2 d\eta + \rho_\infty \bar{u}_\infty^2 (y_\infty - \delta_a / R_s) + p_a y_\infty \right] \quad (\text{A30}) \end{aligned}$$

$$\begin{aligned} \bar{F}_b &= 2\pi x_b \int_0^{y_\infty} \rho_b \bar{u}_b^2 dy + 2\pi x_b \int_0^{y_\infty} p_b dy \\ &= 2\pi x_b \left[(\delta_b / R_s) \int_0^1 \rho_b \bar{u}_b^2 d\eta + \rho_\infty \bar{u}_\infty^2 (y_\infty - \delta_b / R_s) + p_b y_\infty \right] \quad (\text{A31}) \end{aligned}$$

Similarly, the momentum fluxes through the bottom and top of the control volume are:

$$\tilde{F}_o = 2\pi x (\rho_o v_o \tilde{u}_W + \tau_o) \Delta x \quad (\text{A32})$$

$$\tilde{F}_\infty = 2\pi x \rho_\infty v_\infty \tilde{u}_\infty \Delta x \quad (\text{A33})$$

Since the flow is steady in these similarity coordinates, then conservation of momentum requires that the sum of the fluxes equals zero:

$$\sum_i \tilde{F}_i = 0$$

or

$$\tilde{F}_a - \tilde{F}_b + \tilde{F}_o - \tilde{F}_\infty = 0 \quad (\text{A34})$$

Solving the above equation for the streamwise flux yields:

$$(\tilde{F}_a - \tilde{F}_b)/\Delta x = 2\pi x [-\rho_o v_o \tilde{u}_\infty - \tau_o + \rho_\infty v_\infty \tilde{u}_\infty] - 2\pi y_\infty (x_a p_a - p_b x_b)/\Delta x \quad (\text{A35})$$

Taking the limit as Δx approaches zero and using $d\xi = -dx$, we find the momentum conservation law:

$$\frac{d}{d\xi} \tilde{F} = x \rho_o v_o \tilde{u}_W + x \tau_o - x \rho_\infty v_\infty \tilde{u}_\infty - v_\infty \frac{d}{d\xi} x p \quad (\text{A36})$$

where

$$\begin{aligned} \tilde{F} &= x(\delta/R_s) \left[\int_0^1 \rho \tilde{u}^2 d\eta - \rho_\infty \tilde{u}_\infty^2 \right] \\ &= x(\delta/R_s) \int_0^1 (\rho \tilde{u}^2 - \rho_\infty \tilde{u}_\infty^2) d\eta \end{aligned} \quad (\text{A37})$$

But from the mass conservation law (Eq. A12) we recall that

$$\rho_\infty v_\infty = \rho_o v_o - \frac{d}{d\xi} \tilde{F}_m$$

This can be used to eliminate $\rho_\infty v_\infty$ from Equation A36, yielding

$$\frac{d}{d\xi} \tilde{F}_\theta = x \rho_o v_o u_\infty + x \tau_o - v_\infty \frac{d}{d\xi} x p \quad (\text{A38})$$

where

$$\begin{aligned}\tilde{F}_\theta &= \tilde{F} - \tilde{u}_\infty \tilde{F}_m \\ &= x(\delta/R_s) \int_0^1 \rho \tilde{u}(\tilde{u} - \tilde{u}_\infty) d\eta\end{aligned}\quad (\text{A39})$$

The latter represents the surplus momentum flux (relative to the freestream values) created by the boundary layer. The momentum conservation law (Eq. A38) can be nondimensionalized by the momentum flux $\rho_2 u_2^2$, yielding:

$$\frac{d}{d\xi} [x H F^2 \delta_\theta / R_s] = F \dot{m}_o + x H F^2 C_f / 2 - \left(\frac{p_2}{\rho_2 u_2^2} \right) y_\infty \frac{d}{d\xi} x G \quad (\text{A40})$$

where

$$C_f = \tau_o / (0.5 \rho_\infty u_\infty^2) \quad (\text{A41})$$

$$G(x) = p_\infty / p_2 \quad (\text{A42})$$

$$p_2 / \rho_2 u_2^2 = (\gamma - 1) / 2 \quad (\text{A43})$$

In the above, C_f represents the local wall drag coefficient which the fluidized bed exerts on the boundary layer, and $G(x)$ denotes the nondimensional pressure above the boundary layer which can be a function of x . In addition, δ_θ represents the momentum thickness of the boundary layer:

$$\delta_\theta = \delta \int_0^1 h \tilde{f}(\tilde{f} - \tilde{f}_\infty) d\eta \quad (\text{A44})$$

Next, we convert the above integrand to lab-fixed velocity profiles ($f = u/u_\infty$):

$$\begin{aligned}h \tilde{f}(\tilde{f} - \tilde{f}_\infty) &= h (x W_s / u_\infty - f) (1 - f) \\ &= \frac{W_s}{u_2} \frac{x}{F(x)} h(1 - f) - h f(1 - f)\end{aligned}\quad (\text{A45})$$

The expression for the boundary layer momentum thickness then simplifies to:

$$\delta_\theta = I_\theta \delta \quad (\text{A46})$$

where

$$I_\theta(x) = \frac{W_s}{u_2} \frac{x}{F(x)} \int_0^1 h(1 - f) d\eta - \int_0^1 h f(1 - f) d\eta \quad (\text{A47})$$

Using the above relations, the Momentum Integral Equation becomes:

$$\frac{d}{d\xi} [HF^2 I_\theta \delta/R_s] = F\dot{m}_o + HF^2 C_f/2 - \left(\frac{p_2}{\rho_2 u_2^2} \right) (\delta/R_s) \frac{dG}{d\xi} \quad (\text{A48})$$

This equation may be formally integrated to determine the growth in the momentum thickness as a function of ξ :

$$\begin{aligned} \delta_\theta(\xi)/R_s &= I_\theta \delta/R_s \\ &= \int_0^\xi (F\dot{m}_o + HF^2 C_f/2) d\xi / HF^2 \\ &\quad - \frac{p_2}{\rho_2 u_2^2 HF^2} \int_0^\xi (\delta/R_s) \frac{dG}{d\xi} d\xi \end{aligned} \quad (\text{A49})$$

Thus, momentum conservation in the boundary layer demonstrates that the momentum thickness grows because of three effects: mass entrainment, wall drag and exterior pressure gradients.

If the freestream flow is independent of ξ such as in the normal shock case (where $H = F = G = 1$), then the above relations reduce to a particularly simple form:

$$\frac{d}{d\xi} [I_\theta \delta/R_s] = \dot{m}_o + C_f/2 \quad (\text{A50})$$

and

$$\delta_\theta(\xi)/R_s = I_\theta \delta/R_s = \int_0^\xi (\dot{m}_o + C_f/2) d\xi \quad (\text{A51})$$

DISTRIBUTION LIST

DNA-TR-92-17

DEPARTMENT OF DEFENSE

ASSISTANT TO THE SECRETARY OF DEFENSE
ATTN: EXECUTIVE ASSISTANT

DEFENSE INTELLIGENCE AGENCY
ATTN: DB-TPO
ATTN: DIW-4

DEFENSE NUCLEAR AGENCY
ATTN: DDIR G ULLRICH
ATTN: NASF
ATTN: OPNA
ATTN: OTA R ROHR
ATTN: SPSD
ATTN: SPSD LT COL ARTMAN
ATTN: SPSP DR P CASTLEBERRY

2 CYS ATTN: SPWE
ATTN: SPWE C GALLOWAY
ATTN: SPWE T FREDERICKSON
ATTN: SPWE K PETERSON
ATTN: TDTR

2 CYS ATTN: TITL

DEFENSE TECHNICAL INFORMATION CENTER
2 CYS ATTN: DTIC/FDAB

DEPARTMENT OF DEFENSE EXPLORATION SAFETY BOARD
ATTN: CHAIRMAN

FIELD COMMAND DEFENSE NUCLEAR AGENCY
ATTN: FCNV

FIELD COMMAND DEFENSE NUCLEAR AGENCY
ATTN: ENIE N GANTICK
ATTN: FCNM
ATTN: FCTP E MARTINEZ
ATTN: FCTP E RINEHART
ATTN: FCTT

2 CYS ATTN: FCTT W SUMMA

STRATEGIC AND THEATER NUCLEAR FORCES
ATTN: DR E SEVIN

THE JOINT STAFF
ATTN: JKCS

THE JOINT STAFF
ATTN: JAD/SFD

DEPARTMENT OF THE ARMY

DEPARTMENT OF STAFF FOR OPS & PLANS
ATTN: DAMO-SWN

HARRY DIAMOND LABORATORIES
ATTN: SLCIS-IM-TL

U S ARMY ARMAMENT MUNITIONS & CHEMICAL CMD
ATTN: MA LIBRARY

U S ARMY BALLISTIC RESEARCH LAB
2 CYS ATTN: SLCBR-SS-T

U S ARMY CORPS OF ENGINEERS
ATTN: CERD-L

U S ARMY ENGINEER DIV HUNTSVILLE
ATTN: HNDED-SY

U S ARMY ENGINEER DIV OHIO RIVER
ATTN: ORDAS-L

U S ARMY ENGR WATERWAYS EXPER STATION
ATTN: C WELCH CEWES-SE-R
ATTN: CEWES J K INGRAM
ATTN: CEWES-SD J G JACKSON JR
ATTN: J ZELASKO CEWES-SD-R
ATTN: RESEARCH LIBRARY

U S ARMY FOREIGN SCIENCE & TECH CTR
ATTN: AIFRTA

U S ARMY MATERIAL TECHNOLOGY LABORATORY
ATTN: DRXMR J MESCALL
ATTN: TECHNICAL LIBRARY

U S ARMY NUCLEAR & CHEMICAL AGENCY
ATTN: MONA-NU DR D BASH

U S ARMY RESEARCH DEV & ENGRG CTR
ATTN: STRNC-YSD G CALDARELLA

U S ARMY STRATEGIC DEFENSE CMD
ATTN: CSSD-H-SA
ATTN: CSSD-SA-E
ATTN: CSSD-SD-A

U S ARMY STRATEGIC DEFENSE COMMAND
ATTN: CSSD-SA-EV
ATTN: CSSD-SL

U S ARMY WAR COLLEGE
ATTN: LIBRARY

USA SURVIVABILITY MANAGEMENT OFFICE
ATTN: SLCSM-SE J BRAND

DEPARTMENT OF THE NAVY

NAVAL POSTGRADUATE SCHOOL
ATTN: CODE 1424 LIBRARY

NAVAL RESEARCH LABORATORY
ATTN: CODE 2627 TECH LIB
ATTN: CODE 4040 D BOOK
ATTN: CODE 4400 J BORIS
ATTN: CODE 7920 A WILLIAMS

NAVAL SURFACE WARFARE CENTER
ATTN: CODE R44 P COLLINS
ATTN: CODE R44 R FERGUSON

NAVAL WEAPONS EVALUATION FACILITY
ATTN: CLASSIFIED LIBRARY

OFFICE OF CHIEF OF NAVAL OPERATIONS
ATTN: OP 03EG
ATTN: OP 654

OFFICE OF NAVAL RESEARCH
ATTN: CODE 1132SM

DEPARTMENT OF THE AIR FORCE

AERONAUTICAL SYSTEMS DIVISION
ATTN: ENSSS H GRIFFIS

AIR FORCE ENGINEERING & SERVICES CTR/DEMM
ATTN: R FERNANDEZ

AIR UNIVERSITY LIBRARY
ATTN: AUL:LSE

HEADQUARTERS USAF/IN
ATTN: IN

HQ USAF/XOXFS
ATTN: XOXFS

PHILLIPS LABORATORY
ATTN: BLDG 497

STRATEGIC AIR COMMAND/XPSW
ATTN: XPS

WRIGHT RESEARCH & DEVELOPMENT CENTER
ATTN: POTP G SEELY
ATTN: POTX M STIBICH

6510 TW/MAXP
ATTN: P PAUGH

DEPARTMENT OF ENERGY

LAWRENCE LIVERMORE NATIONAL LAB
ATTN: C E ROSENKILDE L-084
ATTN: J BELL L-316
ATTN: L-203 R SCHOCK
ATTN: L-81 R PERRETT

LAWRENCE LIVERMORE NATIONAL LABORATORY
2 CYS ATTN: ALLEN KUHL
2 CYS ATTN: K CHEIN
2 CYS ATTN: R FERGUSON

LOS ALAMOS NATIONAL LABORATORY
ATTN: A S MASON
ATTN: REPORT LIBRARY
ATTN: S S HECKER

MARTIN MARIETTA ENERGY SYSTEMS INC
ATTN: DR C V CHESTER

SANDIA NATIONAL LABORATORIES
ATTN: A CHABAI DIV 9311
ATTN: DIV 5214 J S PHILLIPS
ATTN: DIV 9311 L R HILL
ATTN: TECH LIB 3141

U.S. DEPARTMENT OF ENERGY
OFFICE OF MILITARY APPLICATIONS
ATTN: OMA/DP-252 MAJ D WADE

OTHER GOVERNMENT

CENTRAL INTELLIGENCE AGENCY
ATTN: OSWR/NED

DEPARTMENT OF DEFENSE CONTRACTORS

AEROSPACE CORP
ATTN: H MIRELS
ATTN: LIBRARY ACQUISITION
ATTN: MR LYNCH

APPLIED & THEORETICAL MECHANICS, INC
ATTN: J M CHAMPNEY

APPLIED RESEARCH ASSOCIATES
ATTN: R FLORY

APPLIED RESEARCH ASSOCIATES, INC
ATTN: J KEEFER
ATTN: N ETHRIDGE

APPLIED RESEARCH ASSOCIATES, INC
ATTN: J L BRATTON

APPLIED RESEARCH ASSOCIATES, INC
ATTN: R FRANK

APPLIED RESEARCH ASSOCIATES, INC
ATTN: J L DRAKE

BDM INTERNATIONAL INC
ATTN: E DORCHAK
ATTN: J STOCKTON

BOEING CO
ATTN: E CAMPBELL

CALIFORNIA RESEARCH & TECHNOLOGY, INC
ATTN: J THOMSEN
ATTN: K KREVENHAGEN

CALSPAN CORP
ATTN: M DUNN

CARPENTER RESEARCH CORP
ATTN: H J CARPENTER

E-SYSTEMS, INC
ATTN: TECH INFO CTR

FLUID PHYSICS IND
ATTN: R TRACI

GENERAL ELECTRIC CO
ATTN: K KOCH

GEO CENTERS, INC
ATTN: B NELSON

IIT RESEARCH INSTITUTE
ATTN: DOCUMENTS LIBRARY
ATTN: M JOHNSON

INFORMATION SCIENCE, INC
ATTN: W DUDZIA

INSTITUTE FOR DEFENSE ANALYSES
ATTN: CLASSIFIED LIBRARY

KAMAN SCIENCES CORP
ATTN: L MENTE
ATTN: LIBRARY
ATTN: R RUETENIK

KAMAN SCIENCES CORP
ATTN: J HARPER
ATTN: JOHN KEITH

KAMAN SCIENCES CORP
ATTN: D MOFFETT
ATTN: DASIAC
ATTN: E CONRAD

KAMAN SCIENCES CORPORATION
ATTN: B GAMBILL
ATTN: DASIAC

KTECH CORP
ATTN: E GAFFNEY

LOCKHEED MISSILES & SPACE CO, INC
ATTN: TECH INFO CTR

LOGICON R & D ASSOCIATES
ATTN: C K B LEE
ATTN: D SIMONS
ATTN: LIBRARY
ATTN: R GILBERT
ATTN: T A MAZZOLA

LOGICON R & D ASSOCIATES
ATTN: B KILLIAN
ATTN: E FURBEE
ATTN: J WEBSTER

LOGICON R & D ASSOCIATES
ATTN: G GANONG
ATTN: J WALTON

LOGICON R & D ASSOCIATES
ATTN: E FURBEE
ATTN: J WEBSTER

LOS ALAMOS TECHNICAL ASSOCIATES, INC
2 CYS ATTN: W L CLEMENT

LTV AEROSPACE & DEFENSE COMPANY
2 CYS ATTN: LIBRARY EM-08

MCDONNELL DOUGLAS CORPORATION
ATTN: D JOHNSON
ATTN: L COHEN
ATTN: R HALPRIN

MOLZEN CORBIN & ASSOCIATES, P.A.
ATTN: TECHNICAL LIBRARY

NEW MEXICO ENGINEERING RESEARCH INSTITUTE
ATTN: J JARPE
ATTN: N BAUM
ATTN: R NEWELL

NICHOLS RESEARCH CORPORATION
ATTN: R BYRN

PACIFIC-SIERRA RESEARCH CORP
ATTN: H BRODE
ATTN: L E JOHNSON
ATTN: L SCHLESSINGER

PDA ENGINEERING
2 CYS ATTN: D THEIS
ATTN: J E WUERER

PHYSICAL RESEARCH INC
ATTN: D MODARRESS

PHYSITRON INC
ATTN: M PRICE

RAND CORP
ATTN: B BENNETT

S-CUBED
ATTN: C PETERSEN
ATTN: G SCHNEYER
ATTN: J BARTHEL
ATTN: K D PYATT JR
ATTN: P COLEMAN
ATTN: T PIERCE

S-CUBED
ATTN: C NEEDHAM

SCIENCE APPLICATIONS INTL CORP
2 CYS ATTN: C HSIAO
ATTN: E SWICK
ATTN: F Y SU
ATTN: G EGGUM
ATTN: G T PHILLIPS
ATTN: H WILSON
ATTN: TECHNICAL REPORT SYSTEM

SCIENCE APPLICATIONS INTL CORP
ATTN: DIV 411 R WESTERFELDT

SCIENCE APPLICATIONS INTL CORP
ATTN: J WILLIAMS

SCIENCE APPLICATIONS INTL CORP
2 CYS ATTN: D HOVE
2 CYS ATTN: K SINGER
ATTN: J COCKAYNE
ATTN: W LAYSON

SCIENCE APPLICATIONS INTL CORP
ATTN: K SITES

SCIENCE APPLICATIONS INTL CORP
ATTN: G BINNINGER

SCIENCE APPLICATIONS INTL CORP
ATTN: R ALLEN

SRI INTERNATIONAL
ATTN: D KEOUGH
ATTN: DR B S HOLMES
ATTN: J SIMONS
ATTN: M SANAI

TECHNICO SOUTHWEST INC
ATTN: S LEVIN

**THE TITAN CORPORATION
ATTN: LIBRARY**

**TOYON RESEARCH CORP
ATTN: J CUNNINGHAM**

**TRW SPACE & DEFENSE SECTOR
ATTN: HL DEPT LIBRARY
ATTN: W WAMPLER**

**W J SCHAFFER ASSOCIATES, INC
ATTN: D YOUMANS**

**WASHINGTON STATE UNIVERSITY
ATTN: PROF Y GUPTA**

**WEIDLINGER ASSOC, INC
ATTN: H LEVINE**

**WEIDLINGER ASSOCIATES, INC
ATTN: T DEEVY**

**WEIDLINGER ASSOCIATES, INC
ATTN: I SANDLER
ATTN: M BARON**